

## Research Article

# Chemical Kinetic Study of Nitrogen Oxides Formation Trends in Biodiesel Combustion

Junfeng Yang,<sup>1</sup> Valeri I. Golovitchev,<sup>1</sup> Pau Redón Lurbe,<sup>2</sup> and J. Javier López Sánchez<sup>2</sup>

<sup>1</sup> Department of Applied Mechanics, Chalmers University of Technology, 412-96 Göteborg, Sweden

<sup>2</sup> CMT-Motores Térmicos, Universidad Politécnica de Valencia, 46022 Valencia, Spain

Correspondence should be addressed to Junfeng Yang, jungfeng@chalmers.se

Received 6 December 2011; Accepted 28 February 2012

Academic Editor: Mahesh T. Dhotre

Copyright © 2012 Junfeng Yang et al. This is an open access article distributed under the Creative Commons Attribution License, which permits unrestricted use, distribution, and reproduction in any medium, provided the original work is properly cited.

The use of biodiesel in conventional diesel engines results in increased NO<sub>x</sub> emissions; this presents a barrier to the widespread use of biodiesel. The origins of this phenomenon were investigated using the chemical kinetics simulation tool: CHEMKIN-2 and the CFD KIVA3V code, which was modified to account for the physical properties of biodiesel and to incorporate semidetailed mechanisms for its combustion and the formation of emissions. Parametric  $\phi$ -T maps and 3D engine simulations were used to assess the impact of using oxygen-containing fuels on the rate of NO formation. It was found that using oxygen-containing fuels allows more O<sub>2</sub> molecules to present in the engine cylinder during the combustion of biodiesel, and this may be the cause of the observed increase in NO emissions.

## 1. Introduction

Biodiesel fuels consist of long-chain monoalkyl esters derived from vegetable oils and expected to be increasingly important alternatives or supplements to conventional diesel fuel for use in diesel engines. However, in many studies, as summarized in [1], it was observed that the use of biodiesel in engines causes more NO<sub>x</sub> emissions than are generated when using conventional diesel fuel. Numerous experimental and numerical studies have been conducted in order to better understand the origins of the increased NO<sub>x</sub> emissions, and various explanations have been proposed on the basis of their results; the literature in this area has been reviewed by Mueller et al. [2]. Broadly speaking, two classes of explanation have been put forward: engine calibration effects [3] and combustion effects, such as higher flame temperatures [4, 5], injection timing shifting due to high bulk modulus [6], shorter autoignition delays, or combinations of these factors [2]. While these studies indicate that the increased NO<sub>x</sub> emissions have multiple causes, it is generally accepted that the specific combustion chemistry of biodiesel is probably a major factor. Some of the factors listed have already been shown to have only minor effects on the amount of NO<sub>x</sub> produced, including the adiabatic flame temperature [4]

and the high-bulk modulus of biodiesel [7]. However, the fundamental principles underpinning these increased NO<sub>x</sub> emissions remain elusive, and current experimental techniques have not yet proven to be sufficient for their identification. Consequently, computational modeling of biodiesel spray combustion is an attractive tool for obtaining new insights into the origins of the elevated NO<sub>x</sub> emissions observed when using biodiesel fuels in conventional diesel engines.

To determine the equilibrium compositions and dominant thermal mechanism of NO<sub>x</sub> formation during high-temperature combustion of biodiesel fuels in diesel engines, equilibrium calculations and sensitivity analyses were performed using the EQUIL and PSR codes of the CHEMKIN-2 package [8, 9].

Chemical mechanisms for the combustion of diesel oil surrogate (DOS) and rapeseed methyl ester (RME) have previously been constructed and validated [10, 11]. In order to model the formation of NO<sub>x</sub>, the extended N<sub>2</sub>O/NO/NO<sub>2</sub> submechanism (26 reactions) [12] and the NCN pathway of prompt NO formation (27 reactions) [13] were incorporated into these combustion mechanisms; the modified mechanisms were used in CFD engine simulations of biodiesel spray combustion. The physical and chemical aspects of

the combustion process were simulated using the KIVA3V, Rel. 2 code [14], which couples turbulent flow dynamics with spray atomization described in terms of the Kelvin-Helmholtz/Rayleigh-Taylor, KH-RT, model [15], and accounts for gas and fuel droplets interactions, including droplet collision, evaporation, and mixture formation.

To understand the origins of the increased NO<sub>x</sub> emissions, dynamic  $\phi$ - $T$  parametric maps were constructed for specific species of interest and used in conjunction with data from 3D engine simulations. Analyses of O<sub>2</sub> and NO<sub>x</sub> concentrations revealed that more O<sub>2</sub> (and O atoms) are available during biodiesel decomposition than during that of diesel oil. This is due to the presence of O-atoms in the fuel molecules and indicates that biodiesel combustion tends to occur under more lean mixture conditions than is the case for conventional diesel oil. The calculations indicate that NO concentrations peak at the equivalence ratio of approximately 0.78 exist for both diesel and biodiesel fuels; as such, the slightly leaner fuel/air mixture in the combustion region during combustion of RME might be largely responsible for the increased NO emissions relative to those observed during the combustion of diesel oil.

A similar observation was reported by Adi et al. [16], who claimed that the use of oxygen-containing fuels increases the combustible oxygen mass fraction in the diffusion flame front; this in turn would increase the temperature of combustion, favoring the formation of NO.

Present work addresses to a comparative study between pure diesel oil and neat biodiesel fuel combustion using a numerical method. On the basis of our observations and analyses, we propose the following alternative hypothesis: the use of oxygen-containing fuels such as biodiesel (rather than a pure hydrocarbon fuel such as conventional diesel oil) generates a leaner fuel/air mixture, favoring NO formation. Future studies in this area will focus on analyzing the physical processes involved in the combustion of biodiesel in order to allow for the combustion of this important fuel under lean conditions without the drawback of elevated NO<sub>x</sub> emissions.

## 2. Formulation of the Model

The numerical simulation of combustion phenomena is based on four separate, but coupled topics involving in multiphase combustion systems: the fluid mechanics described by the conservation equation of continuum mechanics, the chemical reactions between species making up the fluid, and spray and droplet dynamics which are the consequence of interaction between liquid fuel and gas. Finally, the systems referred as a set of turbulence modeling equations. The main conservation equations are taken in a form as they are implemented in the 3-D CFD KIVA-3 V code [14]. KIVA, a transient, three-dimensional, multiphase, multicomponent code for the analysis of chemically reacting flows with sprays, has been developed at the Los Alamos National Laboratory. The code uses an arbitrary Lagrangian Eulerian (ALE) methodology on a staggered grid, which discretizes a space using the finite-volume technique. The code uses an implicit time advancement with the exception of the convection

terms that are cast in an explicit, second-order monotone scheme. Also, the convection calculations are sub-cycled in the desired regions to avoid the time step restriction due to Courant conditions. Arbitrary numbers of species and chemical reactions are allowed. A stochastic particle method is used to calculate evaporating liquid sprays, including the effects of droplet collisions and aerodynamics breakups. Although specifically designed for performing ICE calculations, the modularity of the code allows it for easy modifications for solving a variety of combustion problems.

*2.1. The Model Formulation: Main Conservation Laws.* The conservation equations listed below are given in “advective form” rather than in “conservative form” that requires approximations of both the conservative and nonconservative terms:

Conservation of mass:

$$\frac{\partial \rho}{\partial t} + \nabla \cdot (\rho \mathbf{u}) = \dot{\rho}^s. \quad (1)$$

Conservation of momentum (a vector equation with three components):

$$\begin{aligned} \frac{\partial (\rho \mathbf{u})}{\partial t} + \nabla \cdot (\rho \mathbf{u} \mathbf{u}) = \rho \mathbf{g} + \mathbf{F}^s - \frac{1}{a^2} \nabla p \\ + \nabla \cdot \bar{\sigma} - A_o \nabla \left( \frac{2}{3} \rho k \right). \end{aligned} \quad (2)$$

Conservation of energy:

$$\begin{aligned} \frac{\partial (\rho I)}{\partial t} + \nabla \cdot (\rho \mathbf{u} I) = -\nabla \cdot \mathbf{J} + \dot{Q}^c + \dot{Q}^s - p \nabla \cdot \mathbf{u} \\ + (1 - A_o) \bar{\sigma} : \nabla \mathbf{u} + A_o \rho \epsilon. \end{aligned} \quad (3)$$

Conservation of mass for chemical species  $m$  (one equation for each of the  $N_s$  species)

$$\frac{\partial \rho_m}{\partial t} + \nabla \cdot (\rho_m \mathbf{u}) = \nabla \cdot \left[ \rho D \nabla \left( \frac{\rho_m}{\rho} \right) \right] + \dot{\rho}_m^c + \dot{\rho}_m^s \delta_{m1}, \quad (4)$$

where  $m$  is species index,  $N_s$  is the species numbers; superscripts “ $c$ ” and “ $s$ ” denote the terms associated with the chemical reaction and spray, respectively,  $\delta_{i1}$  is the Kronecker delta function, that is, species 1 is the species of which the sprays are composed. The main variable definitions are given in the notations.

The system of conservation laws (1)–(4) is supplemented by equations of state and the algebraic equations specifying the models of fluid, see, for example, [17]. The turbulence was described by the  $k$ - $\epsilon$  model with the velocity dilatation and spray interaction terms.

*2.2. Turbulent Combustion Modeling.* To simulate turbulent combustion, the partially stirred reactor (PaSR) method [18] has been employed. To outline the main features of the approach, let us consider the average gas phase equations (4) for a chemically reacting species. Since the KIVA-3 V code is based on the operation-splitting procedure applied to

the mass conservation equations for species participating in any multistep reaction mechanism, the third step of the computational procedure accounts for chemical kinetics coupled with species micromixing. This step can be interpreted as representing combustion in a constant volume partially stirred reactor of a computational cell size, where reactions occur in a fraction of its volume described in the term of the ODE system:

$$\frac{dc^1}{dt} = \frac{c^1 - c^0}{\tau} = f_r(\dots, c, \dots), \quad (5)$$

where  $\tau$  is a time integration step,  $f_r(\dots, c, \dots) \equiv \rho^c$  is the chemical source term calculated at some unknown (virtual) concentrations,  $c$ , parameters of a subgrid scale reaction zone. The model distinguishes between the concentration (in mean molar density) at the reactor exit,  $c^1$ , the concentration in the reaction zone,  $c$ , and in the feed,  $c^0$ . When time proceeds,  $c^1$  trades place for  $c^0$ . The species indices are omitted for simplicity.

To close the model, the additional equation for the reaction volume can be engaged, that is,

$$\frac{dc}{dt} = -\frac{c - c^1}{\tau_{\text{mix}}} + f_r(c), \quad (6)$$

where  $\tau_{\text{mix}}$  is the micromixing time, the expression for  $f_r(\dots, c, \dots)$  is formally simplified.

The difference between (6) and that from the PSR perfectly stirred reactor (PSR) [9] model is that the residence time in the reactor equation of the PSR model is replaced by the micromixing time. Taking this equation in a steady-state form, one can get the basic equations of the PaSR model (6) as follows:

$$\frac{dc^1}{dt} = f_r(c) = \frac{c - c^1}{\tau_{\text{mix}}}. \quad (7)$$

There are a number of micromixing models based on different principles; the review of these can be found in [19]. One of the simplest and widely used micromixing models is the "interaction by exchange with the mean" (IEM) approach [19]. In this approach, the scalar variable  $c$  relaxes to its mean  $c^1$  value according to the linear term in (7). Then, rewriting the reaction rate in (7),  $f_r(c)$ , in terms of reactor exit parameters, one can get

$$f_r(c^1) + \left( \frac{\partial f_r}{\partial c} \right)_{|c=c^1} (c - c^1) = f_r(c^1) - \frac{c - c^1}{\tau_c} \quad (8)$$

using the Taylor's expansion at the value  $c^1$ , assuming that the reaction times can be estimated as reciprocal values of the Jacobian matrix diagonal elements evaluated at the grid resolved values  $c = c^1$ , that is,  $\tau_c \sim [\partial f_r / \partial c]^{-1}$  and accounting for that  $(\partial f_r / \partial c)_{|c=c^1} < 0$ . Algebraic manipulation with the second pair of (4) leads to the relation:

$$f_r(c^1) - \frac{c - c^1}{\tau_c} = \frac{c - c^1}{\tau_{\text{mix}}}. \quad (9)$$

and, finally, to the main relation of the PaSR model:

$$f_r(c) = f_r(c^1) \frac{\tau_c}{\tau_c + \tau_{\text{mix}}}. \quad (10)$$

This means the chemical source terms can be calculated using the averaged species concentrations, if multiplied by the model rate parameters ratio  $\tau_c / (\tau_c + \tau_{\text{mix}})$ . The application of (10) is applicable to the chemical mechanisms of an arbitrary complexity. The model parameters such as  $\tau_{\text{mix}}$  and  $\tau_c$  are calculated as described in [20, 21], for example,

$$\tau_{\text{mix}} = \left( \frac{k}{\varepsilon} \right) \cdot \left( \frac{c_\mu}{\text{Re}_t} \right)^{0.621}, \quad (11)$$

where  $\text{Re}_t$  is the turbulence Reynolds number,  $c_\mu$  is the parameter of the  $k$ - $\varepsilon$  model.

It is instructive to note that the rate expression (10) treats the reactions in a full complexity on the contrary to the expression used in the "characteristic time" of combustion [22]:

$$f_{r,i}(c) = -\frac{Y_i - Y_i^*}{\tau_{c,i} + f \tau_{\text{mix}}}, \quad (12)$$

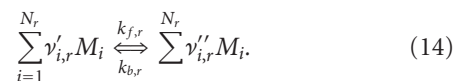
where  $Y_i$  and  $Y_i^*$  are current and equilibrium concentrations,  $f$  is a multiplier ranging from 0 to 1 switching from kinetic to turbulent regime of combustion, and characteristic chemical time is taken as the ignition delay time calculated using detailed chemical mechanism.

Sometimes, on the ignition stage of combustion, the shell ignition model which operates with artificial species representing low-temperature chemistry is used. The review of turbulence combustion models can be found in [23], but if the ignition is formally considered as the process preceding the combustion stage, such models are not used in the ignition description. The most effective separation of ignition and combustion stages is realized in [24] based on the usage of ignition integral calculated with the help of an artificial neural network (ANN) and KIVA-3 V (or KIVA4) code. The ignition integral:

$$I(t) = \int_0^t \frac{1}{\tau_{\text{ign}}(T, p, \phi)} dt \quad (13)$$

predicts the ignition onset as  $I(t) = 1$  using a time history of ignition delays during the process development. The ignition delays are calculated and stored in a special library using the detailed chemical mechanisms for particular fuels.

**2.3. Finite-Rate Formulation for Reaction Model.** If the effects of turbulent fluctuations are ignored, the reaction rates can be determined by the Arrhenius rate expressions. Consider the  $r$ -reaction written in a form as follows:



The molar rate of creation/destruction of  $i$ -species in to  $r$ -reaction is given by

$$\hat{R}_{i,r} = \Gamma (\nu'_{i,r} - \nu''_{i,r}) \left( k_{f,r} \prod_{j=1}^{N_r} [C_{j,r}]^{\eta'_{j,r}} - k_{b,r} \prod_{j=1}^{N_r} [C_{j,r}]^{\eta''_{j,r}} \right). \quad (15)$$

Above,  $\Gamma$  represents the net effect of inert collision partners in the third body reactions on the reaction rate. This term is read as

$$\Gamma = \sum_j^{N_r} \gamma_{j,r} C_j, \quad (16)$$

where  $\nu'_{i,r}$  are stoichiometric coefficients for reactants in  $r$ -reaction,  $\nu''_{i,r}$  are stoichiometric coefficients for product in  $r$ -reaction,  $M_i$  denoting  $i$ -species,  $k_{f,r}$  is a rate parameter for the forward stage of reaction  $r$ ,  $k_{b,r}$  is a rate parameter for the backward stage of reaction  $r$ ,  $C_j$  are molar concentrations of reactants and products in  $r$ -reaction.  $\eta'_{j,r}$  are forward rate exponents for reactant and product species,  $\eta''_{j,r}$  are backward rate exponents for reactant and product species, and  $\gamma_{j,r}$  are the third body efficiencies of the  $r$ -reaction. For elementary reactions,  $\eta_{jr}$  are equal to  $\nu_{j,r}$ ; for global reactions, these values are specified based on the experiment rate data.

The formulation of chemical kinetics problem must be supplemented by the equation of stages for ideal and thermally perfect gas. The thermodynamic properties required for the calculations are available from the database [25].

**2.4. Mechanisms of  $\text{NO}_x$  Formation.** In order to understand the increased emissions of  $\text{NO}_x$  during biodiesel combustion, it is necessary to understand the key reactions in the formation of  $\text{NO}_x$ . Over the last few decades, many scientific and technical articles concerning the formation of  $\text{NO}_x$  have been published. On the basis of these studies, four main processes that form nitric oxides have been identified, as summarized by Miller and Bowman [26]: the thermal, prompt,  $\text{N}_2\text{O}$ , and fuel-bound nitrogen mechanisms.

The thermal mechanism of  $\text{NO}$  formation was proposed by Zeldovich et al. and involves a series of elementary reactions [27, 28] with high activation energies due to the strength of the triple bond in the  $\text{N}_2$  molecule, which can only be broken at an appreciable rate at very high temperatures. This mechanism is generally accepted to play a major role in the formation of  $\text{NO}_x$ . Obviously, the rate of the Zeldovich mechanism is highly sensitive to the temperature of the reactants in flames, and to the concentrations of O and N atoms. In diesel engines, the in-cylinder and flame temperatures are determined by the properties of the liquid fuel (such as its bulk modulus and cetane number), the thermal-physical properties of the vapor (enthalpy, heat capacity), and the rate of heat loss, which is primarily due to radiation from soot particles. The radical O could originate from the oxidizer ( $\text{O}_2$ ) and oxygenated fuel molecules; the only possible source of nitrogen is the air. An extended Zeldovich mechanism that takes all of these key factors into

account was used in this study; the key elementary steps in this mechanism are reactions 1–4 in Table 1, which were supplemented with the reactions of the  $\text{N}_2\text{O}$  pathways (reactions 5–9) and elementary steps corresponding to the “catalytic” interaction between  $\text{NO}$  and  $\text{NO}_2$  (reactions 10–14). Data on the rates of these reactions were taken from the literature [12] and used without modification.

The nitrous oxide ( $\text{N}_2\text{O}$ ) mechanism, first postulated by Wolfrum [29], is analogous to the Zeldovich mechanism in that its key step involves an O atom attacking molecular nitrogen in the presence of third body to form  $\text{N}_2\text{O}$ , which can subsequently react with O to produce  $\text{NO}$ . This mechanism is generally considered to play a minor role in the overall formation of  $\text{NO}$  [30]. Initially, Tomeczek and Gradon [31, 32] proposed rate parameters much higher than those that are currently used, resulting in the overprediction of  $\text{NO}$  concentrations in  $\text{CH}_4\text{-O}_2\text{-Ar}$  flames [33]; more experimental data will be needed in order to obtain accurate rates for this process. The nitrous oxide mechanism is typically regarded as being a thermal  $\text{NO}$  formation mechanism; the combination of this mechanism with the Zeldovich mechanism is referred to as the thermal  $\text{NO}/\text{N}_2\text{O}$  route.

The prompt  $\text{NO}$  mechanism was suggested by Fenimore [34]. Its main feature is that the  $\text{CH}$  radical (methylidyne), which is formed exclusively at the flame front, reacts with nitrogen in the air to form hydrocyanic acid ( $\text{HCN}$ ), which reacts further to form  $\text{NO}$  [34]. However, predictions of the rate of  $\text{NO}$  formation via processes that involve  $\text{HCN}$  are typically relatively inaccurate.  $\text{NCN}$ -based prompt  $\text{NO}$  formation has recently been observed in gaseous jet combustion [35] and has been proposed to play a role in the combustion of methane [36, 37]; it was subsequently incorporated into a detailed mechanism for methane combustion [13]. The  $\text{NCN}$  pathway of prompt  $\text{NO}$  formation involves the 27 elementary steps that are listed in Table 2, along with the relevant rate parameters. It is important to note that both the  $\text{HCN}$  and the  $\text{NCN}$ -based prompt  $\text{NO}$  mechanisms are favored in rich flames. However, because the only available data on the rates of the relevant reactions had been obtained at atmospheric pressure, the prompt  $\text{NO}$  mechanism was not considered in previous studies [2]; little is known about the rates of these processes under the conditions that prevail during the combustion of diesel oil. Moreover, the prompt  $\text{NO}$  mechanism was considered to be unimportant because combustion in diesel engines generally occurs under lean conditions, which suppress the formation of  $\text{CH}_x$  radicals and are thus unfavorable to the prompt  $\text{NO}$  mechanism. However, while the combustion process in diesel engines is lean on the overall, localized regions of rich combustion occur in non-premixed fuel/air flames. As such, to properly understand the production of  $\text{NO}_x$  in diesel engines, it is necessary to determine the contribution of the prompt  $\text{NO}$  mechanism. To the best of our knowledge, the work described herein was the first study on the impact of the prompt  $\text{NO}$  mechanism on the production of  $\text{NO}_x$  during the combustion of biodiesel fuels.

Fuel-bound nitrogen has been shown to affect the formation of  $\text{NO}_x$  during the combustion of nitrogen-containing compounds. For example, during the gasification process,

TABLE 1: Elementary steps in the thermal mechanism of NO and N<sub>2</sub>O. The forward reaction rate is given by  $k_f = A_f T^{n_f} \exp(-E_f/RT)$  [12].

		$A_f$	$n_f$	$E_f$
1	$N + NO = N_2 + O$	$3.50E + 13$	0.0	330
2	$N + O_2 = NO + O$	$2.65E + 12$	0.0	6400
3	$N + OH = NO + H$	$7.33E + 13$	0.0	1120
4	$N + CO_2 = NO + CO$	$1.90E + 11$	0.0	3400
5	$N_2O + O = N_2 + O_2$	$1.40E + 12$	0.0	10810
6	$N_2O + O = NO + NO$	$2.90E + 13$	0.0	23150
7	$N_2O + H = N_2 + OH$	$4.40E + 14$	0.0	18880
8	$N_2O + OH = N_2 + HO_2$	$2.00E + 12$	0.0	21060
9	$N_2O + M = N_2 + O+M$	$1.30E + 11$	0.0	59820
10	$NO + HO_2 = NO_2 + OH$	$2.11E + 12$	0.0	-480
11	$NO_2 + O = NO + O_2$	$3.90E + 12$	0.0	-240
12	$NO_2 + H = NO + OH$	$1.32E + 14$	0.0	360
13	$NO + O + M = NO_2 + M$	$1.06E + 20$	-1.41	0.0
14	$NO_2 + CH_3 = CH_3O + NO$	$1.50E + 13$	0.0	0.0
15	$NO + CH_3O_2 = NO_2 + CH_3O$	$2.53E + 12$	0.0	-358

TABLE 2: Elementary steps in the NCN pathway of prompt NO formation. The forward reaction rate is given by  $k_f = A_f T^{n_f} \exp(-E_f/RT)$  [13].

		$A_f$	$n_f$	$E_f$
1	$CH + N_2 = CN + H$	$3.0E + 12$	0.0	22155
2	$CN + N_2O = CN + NO$	$6.0E + 13$	0.0	15360
3	$CN + N_2O = NCN + NO$	$1.80E + 10$	0.0	1450
4	$CN + NCO = CN + CO$	$1.8E + 13$	0.0	0.0
5	$C_2O + N_2 = CN + CO$	$7.0E + 11$	0.0	17000
6	$CH + N_2 = HNCN$	$1.65E + 21$	-3.62	14196
7	$HNCN + M = H + CN + M$	$1.79E + 28$	-3.44	64502
8	$HNCN + O = NO + HCN$	$1.22E + 14$	0.05	73.5
9	$HNCN + O = NH + NCO$	$5.6E + 13$	0.05	73.5
10	$HNCN + O = CN + HNO$	$9.36E + 12$	0.05	73.5
11	$HNCN + OH = CN + H_2O$	$8.28E + 03$	2.78	3135
12	$HNCN + O_2 = HO_2 + CN$	$1.26E + 08$	1.28	24240
13	$NCN = N + CN$	$2.95E + 30$	-5.29	117090
14	$NCN = C + N_2$	$2.66E + 28$	-5.23	83110
15	$NCN = CNN$	$3.69E + 29$	-5.84	78410
16	$NCN + H = HCN + N$	$1.89E + 14$	0.0	8425
17	$NCN + O = CN + NO$	$2.54E + 13$	0.15	-34
18	$NCN + O = CO + N_2$	$2.42E + 02$	2.32	-1135
19	$NCN + O = N + NCO$	$2.2E + 09$	0.42	-157
20	$NCN + N = N_2 + CN$	$1.0E + 13$	0.0	0.0
21	$NCN + C = CN + CN$	$1.0E + 13$	0.0	0.0
22	$NCN + OH = HCN + NO$	$3.32E + 10$	-0.97	7290
23	$NCN + OH = HCN + NO$	$4.69E + 10$	0.44	4000
24	$NCN + O_2 = NO + NCO$	$3.8E + 09$	0.51	24590
25	$NCN + CH = HCNCN$	$3.21E + 13$	0.0	-860
26	$NCN + CN = C_2N_2 + N$	$1.25E + 14$	0.0	8020
27	$NCN + CH_2 = H_2CN + CN$	$7.99E + 13$	0.0	4630

nitrogenous compounds in coal give rise to ammonia (NH<sub>3</sub>) and hydrocyanic acid (HCN), which are then oxidized to NO [30]. However, biodiesel fuels are mixtures of long-chain methyl esters and as such are considered to be nitrogen free, meaning that it is not necessary to consider the effects of fuel-bound nitrogen when modeling their combustion. Moreover, contemporary manufacturing techniques make it possible to ensure that the fuel's nitrogen content remains negligible.

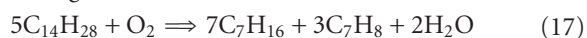
In addition to these four major routes for NO<sub>x</sub> formation, there are several unverified mechanisms, for example, diazomethane, CH<sub>2</sub>N<sub>2</sub>, [38], NNH [39], and stepwise N<sub>2</sub>H<sub>3</sub> [40] routes. Since all of these mechanisms either require further experimental validation or have yet to demonstrate their relevance experimentally, they were not considered in the study reported herein.

This article describes a study of the contributions of two verified mechanisms of NO formation (the thermal NO/N<sub>2</sub>O and NCN-based prompt NO mechanisms) to the elevated NO<sub>x</sub> emissions observed during the combustion of biodiesel, using numerical methods. In particular, calculations of the chemical kinetics of combustion and simulations of diesel engine behavior were performed. Parametric  $\phi$ - $T$  maps were constructed on the basis of the simulated results, leading to a plausible explanation for the increased NO<sub>x</sub> emissions.

**2.5. Combustion Mechanisms.** The combustion mechanisms of real hydrocarbon fuels involve a lot of species and chemical reactions. In order to accurately model complex chemical phenomena, it is necessary to use validated detailed and reduced mechanisms. The reduced chemical mechanisms used in CFD studies are simplifications of the (more realistic) detailed mechanisms. The earliest models used a series of one-step reactions to describe the conversion of fuel to products (water and carbon dioxide in the simplest case). This mechanism is normally called the global reaction mechanism, and it is not widely used nowadays because of its poor accuracy. However, some elements of the approach are retained in the mechanisms based on so-called surrogate fuel components, which are used to represent real fuels.

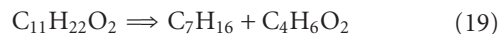
The work described herein focused on three surrogate fuel components and their associated combustion mechanisms: diesel oil surrogate (DOS) [10], rapeseed methyl ester (RME) [11], and palm-oil methyl ester (PME) [41].

**2.5.1. The Diesel Oil Surrogate Mechanism.** The practical diesel oil consist of a great number of aliphatic, cyclic, and aromatic compounds, and their combustion is too complex to be modeled using a comprehensive set of chemical reaction mechanism for each constituent. Consequently, a diesel oil surrogate model was proposed, as is a 70/30% mixture of *n*-heptane (C<sub>7</sub>H<sub>16</sub>) and toluene (C<sub>7</sub>H<sub>8</sub>) to achieve the same C/H proportion and cetane number as real diesel oil [10]. Both components of the mixture can be formed by the pyrolysis of C<sub>14</sub>H<sub>28</sub>, which is taken to be representative of a "real" diesel molecule; a global oxidative pyrolysis step, shown in (17), was added to the combustion mechanism to account for the decomposition of this molecule into the components of the surrogate mixture:



The *n*-heptane and toluene represent the aliphatic and aromatic compounds of real diesel oil, respectively. The DOS combustion mechanism involves 68 species participating in 280 reactions. The physical properties of DOS are assumed to the combination as real diesel oil heat of formation, density, vapor pressure, and thermal conductivity; the enthalpy is set equal to that of *n*-dodecane, and the critical temperature, latent heat, liquid viscosity, and surface tension are set equal to those for *n*-hexadecane [13]. The DOS mechanism has been validated against shock-tube autoignition delays measured at different pressures, temperatures, and equivalence ratios [10]. It has been used in 3D CFD simulations of diesel engines that generated predictions of the in-cylinder parameters which were in a good agreement with experimental data [10].

**2.5.2. The RME Combustion Mechanism.** The RME combustion mechanism was generated by combining the DOS, reduced mb (methyl butanoate), and md (methyl decanoate) submechanisms [11, 42, 43]. The first step of the mechanism involves the decomposition of methyl oleate (C<sub>19</sub>H<sub>36</sub>O<sub>2</sub>), a major component of real RME fuel, into md (C<sub>11</sub>H<sub>22</sub>O<sub>2</sub>), mb (C<sub>5</sub>H<sub>10</sub>O<sub>2</sub>), and allene (C<sub>3</sub>H<sub>4</sub>) in a molar ratio of 1 : 1 : 1; see (18). The md then decomposes into *n*-heptane and mp2d (C<sub>4</sub>H<sub>6</sub>O<sub>2</sub>), an intermediate in the combustion of md and mb, as as follows:



The oxidation pathway for the above substituent component was illustrated in Figure 1. The route for mb oxidation involves a series of hydrogen-abstract, oxygen-addition to the radical methyl esters, isomerization and ketohydroperoxide decomposition, Figure 1(a). The md decomposes into mp2d and *n*-heptane, see Figure 1(b). The submechanism of mp2d was already considered in the mb mechanism. The oxidation of *n*-heptane was only depicted for the pathway of H-abstraction and the decomposition of *n*-heptyl radical for clarity. The oxidation of allene is in a more straightforward way to the final products and low level intermediates (e.g., CH<sub>2</sub>O, H<sub>2</sub>O, C<sub>2</sub>H<sub>4</sub>) but less subbranch reactions, Figure 1(c).

The physical and thermal properties of RME are taken to be identical to those of methyl oleate [25, 44]. The final reduced RME combustion mechanism features 98 species and 450 reactions and was validated against experimental data obtained using a Volvo D12C diesel engine [11].

**2.5.3. The PME Combustion Mechanism.** PME oxidation is represented by the detailed methyl palmitate, MP, mechanism, which features 4222 species and 41573 reactions and was automatically generated using the EXGAS software package [41]. It has been validated against the measured conversion rates of methyl dodecanoate in a jet-stirred reactor, and the rules used when generating it have been described in detail [41]. The skeletal reaction diagram shown in Figure 2 illustrates the main pathway in the oxidation of PME.

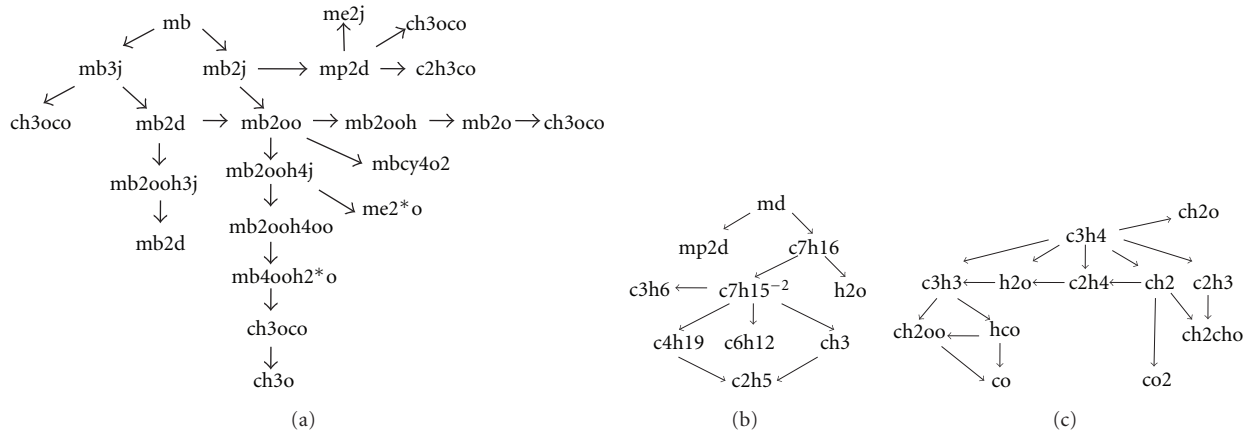


FIGURE 1: The oxidation pathway analysis for substituent components (a) methyl butanoate,  $C_5H_{10}H_2$ , (b) methyl decanoate,  $C_{11}H_{22}O_2$ , (c) allene,  $C_3H_4$ .

As shown, the MP molecule decomposes into low level methyl esters and olefin radicals directly via  $\beta$ -scission of the C–C bonds at high temperatures. Conversely, under low-temperature conditions, oxidation is initiated by hydrogen atom abstraction caused by collisions between fuel and small radicals such as O, H, or OH. The addition of oxygen allows fuel radicals to form the peroxy methyl ester radical, which can undergo isomerization reactions and then decompose into ketones or cyclic ethers or undergo another addition of oxygen to form ketohydroperoxides. Ketohydroperoxides decompose then into two radicals providing chain branching to consume the  $C_{17}$  molecules. The thermodynamic properties of the most species involved were calculated using the THERGAS code and stored in CHEMKIN-2 format [45]. Properties of some species were taken from Burcat's data compilation [25]. The kinetic data for the chemical reactions, for example, isomerizations, combinations, and unimolecular decompositions, are calculated using KINGAS sub-package [45]. The detailed PME combustion mechanism is too large, that prevents its use in 3D CFD studies. The mechanism has been used in 0D calculations only, for example, for the analysis of autoignition and chemical equilibrium.

In order to study  $NO_x$  formation, the all thermal NO and  $N_2O$  submechanisms and the NCN pathway of prompt  $NO_x$  formation were incorporated into each of these three mechanisms. The prompt NCN-based  $NO_x$  mechanism, which features 24 elementary steps, was adapted from Konnov's mechanism number 0.6 [13] without modification.

**2.6. Chemical Equilibrium/Kinetics Calculations.** At equilibrium, the reactant concentrations do not change over time and the state parameters (temperature, pressure, and mixture composition) are determined by the species' thermal properties, that is, their enthalpies, entropies, and heat capacities. The equilibrium temperature (and thus, by definition, the adiabatic flame temperature) and equilibrium NO concentration can be predicted using 0D calculations, which are sufficiently fast to be performed using detailed mechanisms and provide an overview of the correlations between

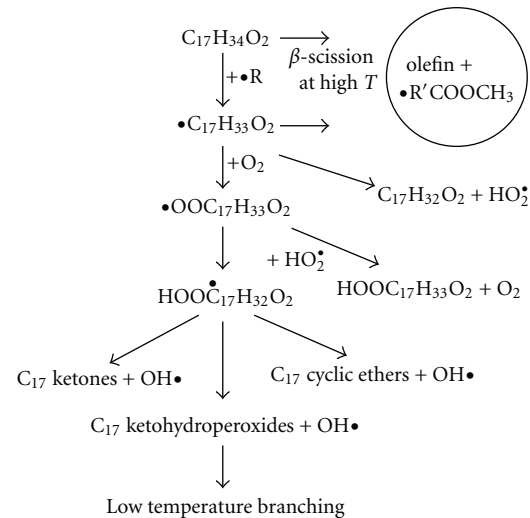


FIGURE 2: The skeletal reaction pathways for the oxidation of PME.

the factors that affect NO formation. To this end, the EQUIL code [8] of the CHEMKIN-2 package was used to calculate the composition and temperature of the equilibrium mixture, in terms of the concentrations of species such as NO,  $CH_2$ , and CH. The flame temperature is a particularly useful property because of the pronounced temperature dependence of thermal NO formation. Particular attention was paid to the concentrations of the methylidyne/methylene radicals (CH and  $CH_2$ ) because they are involved in the initiation of the prompt NO reactions. For illustrative purposes, the EQUIL analysis was performed for the DOS, RME, and PME fuels, assuming an initial pressure of 3000 kPa, an initial temperature of  $626.84^\circ C$ , and allowing the equivalence ratio to vary in the range  $\phi = 0.1-9$ , in a constant volume system.

To identify the reactions that have the most significant effects on the rate of NO formation, 0-D calculations were performed using the perfectly stirred reactor (PSR) model [9] as implemented in the CHEMKIN-2 package. The PSR model assumes the mixing of the oxidant and fuel to be

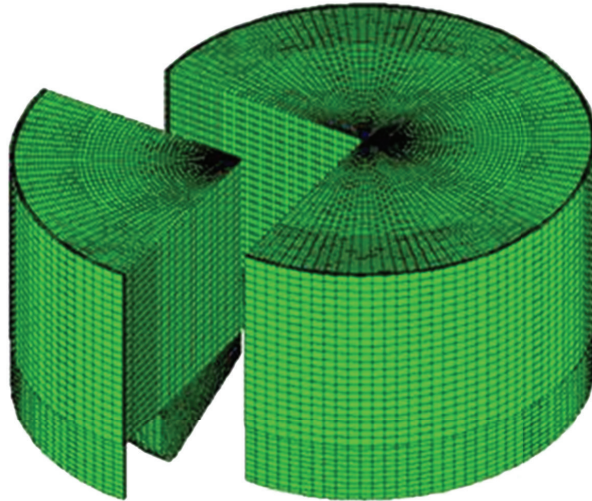


FIGURE 3: The full computational mesh for the Volvo D12C diesel engine, comprising 400,774 cells, and a 72-degree sector mesh with ~80,000 cells at BDC.

infinitely fast and the reactor parameters to be spatially uniform. Therefore, during the mixture's residence time in the reactor, combustion proceeds under chemical control. This assumption provides a convenient platform for studying the formation and emission of species such as NO using inherent sensitivity analysis. The sensitivity coefficients indicate the most sensitive chemical reactions in the various NO-forming pathways that are operational at different temperatures. To simulate the isothermal system used in experiments, a diluted fuel mixture (fuel:N<sub>2</sub>, 0.3:99.7) and an oxidizer mixture (O<sub>2</sub>:N<sub>2</sub>, 21:79) were injected through the inlet port at constant ambient pressure and different initial temperatures (1226.84°C, 1526.84°C, and 2026.84°C). The equivalence ratio was assumed to be 0.5 that is regarded as a typical averaged  $\phi$  value for the diesel engine combustion.

**2.6.1. 3D Diesel Engine Modeling.** 3D CFD diesel engine modeling was used to investigate the impact of biodiesel fuel on the amount of NO<sub>x</sub> emitted via the exhaust during normal operation of the engine. The engine modeled in this paper is the one-cylinder, direct injection Volvo D12C research engine with a displacement volume of 2 L. The engine has an axisymmetric bowl-in-piston geometry with a peak at the centre of the bowl and a five-hole injector placed vertically in a central region of the cylinder. The relevant engine specifications (geometry and operating conditions) are listed in Table 3. A full 360° mesh comprised nearly 400,000 cells and a 72° sector mesh consisting of ~80,000 cells at Bottom Dead Center, BDC, was used in the modeling studies, as shown in Figure 3. The full- and sector-engine meshes were constructed using the K3PREP preprocessor embedded in the KIVA3V code. A partial engine cycle (starts from Inlet Valve Close, ~-160 CAD ATDC (Crank Angle Degree After Top Dead Center), up to 120 CAD ATDC, by which point the combustion process has gone to completion) was analyzed using the 3D CFD model based on the KIVA3V

TABLE 3: The specifications and operating conditions of the Volvo D12C diesel engine.

Bore	131 mm
Stroke	150 mm
Squish	1.85 mm
Connecting rod	260 mm
Injector nozzle dia ( $\varnothing$ )	0.235 mm
Engine speed	1000 rpm
Start of injection	-5.5 CAD ATDC
Injection duration	9.2 CAD
Injection mode	Main
Injected mass/stroke	$60.8 \times 10^{-6}$ kg
Initial pressure	103 kPa
Initial temp	56.84°C
Included angle of spray	145 deg
Spray cone 1/2 angle	12.5 deg
Initial droplet temp	76.84°C

code coupled with semidetailed combustion chemistry kinetics for DOS and RME fuels. The computational submodels implemented in the code to treat diesel spray combustion processes are listed in Table 4.

**2.6.2. Parametric  $\phi$ -T Maps.** The use of static  $\phi$ -T maps [46] and simplified combustion models in 3D engine simulations makes the results of such analyses more comprehensive. We present the results of an extended analysis based on detailed chemical modeling of the combustion of biodiesel fuels. These maps can be described as being "dynamic" [47], because the pressures and elapsed times after fuel injection used when plotting the parametric regions are continuously updated and correspond to the values calculated by the 3D

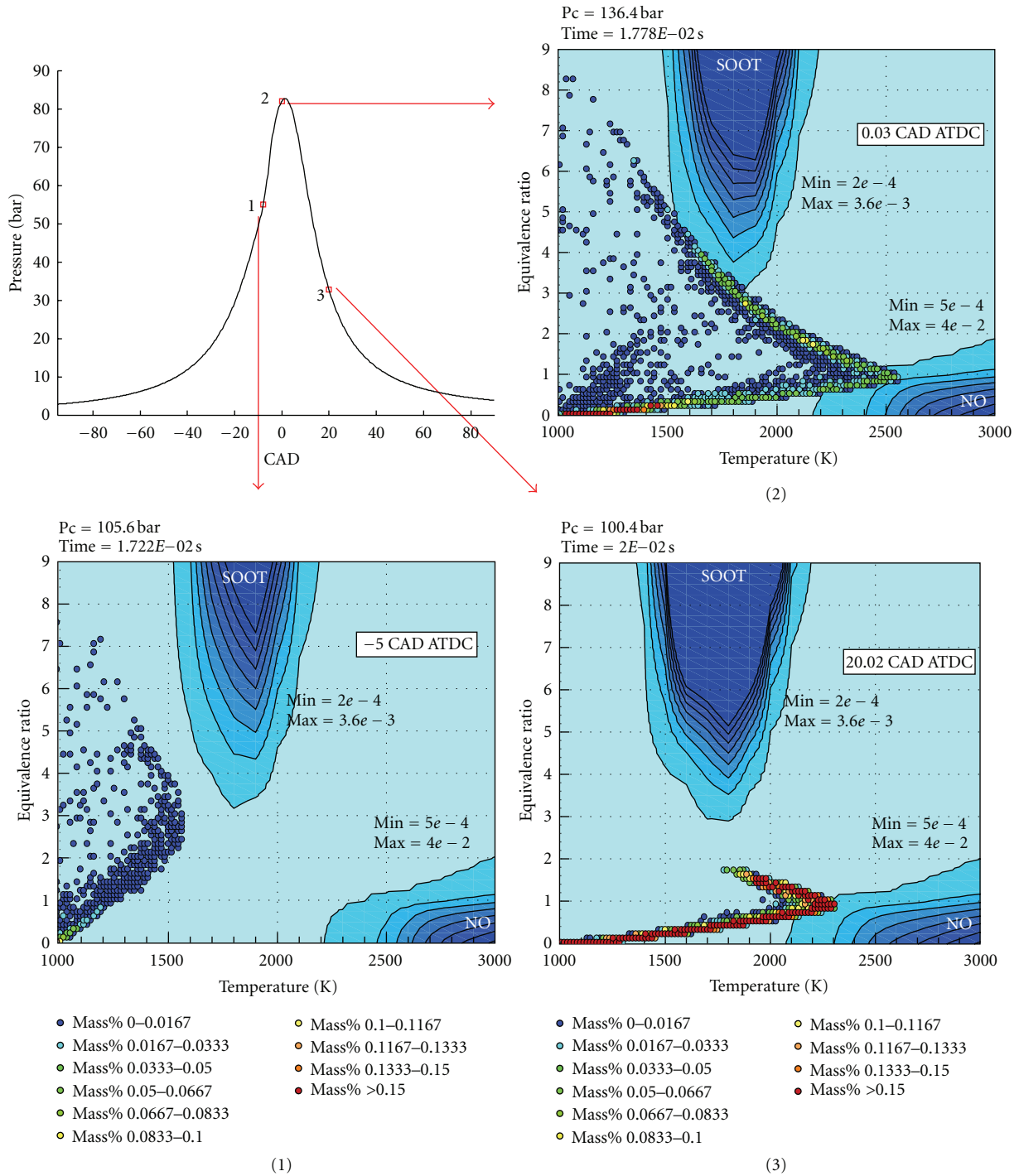


FIGURE 4: Schematic showing the construction of parametric  $\phi$ -T dynamic maps. Maps 1–3 correspond to different points on the compression/expansion pressure curve.

engine simulation (see Figure 4). The points plotted on the maps represent the  $\phi$ -T values of in-cylinder cells, while the species mass fraction corresponding to each  $\phi$ -T region is labeled by its color. The positions of these points on the emissions maps provide useful insights into the complex relationships between combustion and the formation of emissions. The kinetic calculations were carried out using a special

option, TTIM, of the SENKIN code [48] of the CHEMKIN-2 package.

The equivalence ratio, one of the key parameters in the map, needs to be treated carefully when dealing with oxygenated fuels such as biodiesel. The approach used when calculating the value of  $\phi$  for hydrocarbon fuels such as DOS is straightforward, as discussed elsewhere [47, 49]. When

TABLE 4: The computational submodels encoded in the KIVA3V, Rel. 2 code.

Turbulence model	RNG $k$ - $\epsilon$ model
Breakup model	Hybrid KH-RT model
Collision model	Coalescence/grazing
Turbulent dispersion model	Gaussian probability distribution
Spray/wall interaction model	Particle method
Heat transfer model	Improved Law-of-Wall model
Evaporation model	Single component fuel
Combustion model	Detailed Arrhenius kinetics
Turbulence/chemistry interaction	PaSR model
Soot model	HACA pathway and simplified surface kinetics
NO <sub>x</sub> formation model	Thermal and prompt NO

TABLE 5: Oxidation numbers of elements of interest in the saturated stoichiometric products [49].

Element	Oxidation number
Carbon, C	+4
Hydrogen, H	+1
Oxygen, O	-2
Nitrogen, N	0

dealing with oxygenated fuels, however, it is necessary to consider the oxygen atoms present in the fuel molecules. The chemical equivalence ratio was defined on the basis of the oxidation states of the elements in the fuel [49]:

$$r = - \frac{\left[ \sum_{i=1}^{\text{NLM}} V_i^+ b_i \right]}{\left[ \sum_{i=1}^{\text{NLM}} V_i^- b_i \right]}, \quad (20)$$

where  $V_i^+$  and  $V_i^-$  are positive and negative oxidation states of the  $i$ th element in the relevant species (see Table 5). At least one of these states must be zero.

For example, if the negative oxidation state for oxygen is equal to  $-2$ , its positive oxidation state is zero. The values of  $b_i$  in expression (20) are given by

$$b_i = \sum_{k=1}^{\text{NS}} a_{ik} n_k \quad (i = 1, \dots, \text{NLM}, k = 1, \dots, \text{NS}), \quad (21)$$

where NLM is the number of elements, NS is the number of species,  $a_{ik}$  is the number of kg-atoms of element per kg-mole of species  $k$ , and  $n_k$  is the kg-mole number of species  $k$  in the mixture, (kg-mole)/kg.

Equation (20) thus differs from the conventional fuel to oxygen equivalence ratio:

$$\phi = \frac{f/o}{(f/o)_{\text{st}}}, \quad (22)$$

where  $(f/o)_{\text{st}}$  is the fuel/oxygen mass ratio under stoichiometric conditions.

Equation (22) is applicable to hydrocarbon-air mixtures before combustion has begun. When dynamic maps are constructed, the initial mixture composition is always represented by reactants and combustion products exported from the previous stages. Under such conditions, (22) is not applicable, but (20) can be used to characterize the mixture's stoichiometry. It can be shown that the two equivalence ratios  $r$  and  $\phi$  are identical under stoichiometric conditions. They also take the identical values when considering the initial mixture consisting of only fuel and oxygen; this can be demonstrated by considering the example of RME, C<sub>19</sub>H<sub>36</sub>O<sub>2</sub>, for which

$$\begin{aligned} r &= - \frac{\left[ \sum_{i=1}^{\text{NLM}} V_i^+ \sum_{k=1}^{\text{NS}} a_{ik} n_k \right]}{\left[ \sum_{i=1}^{\text{NLM}} V_i^- \sum_{k=1}^{\text{NS}} a_{ik} n_k \right]} \\ &= \frac{4 \cdot 19 \cdot n_{\text{fu}} + 1 \cdot 36 \cdot n_{\text{fu}} - 2 \cdot 2 \cdot n_{\text{fu}}}{2 \cdot 2 \cdot n_{\text{ox}}} \quad (23) \\ &= 27 \frac{n_{\text{fu}}}{n_{\text{ox}}} = \frac{n_{\text{fu}}/n_{\text{ox}}}{(n_{\text{fu}}/n_{\text{ox}})_{\text{st}}}. \end{aligned}$$

Here,  $(n_{\text{fu}}/n_{\text{ox}})_{\text{st}} = 1/27$  for the RME fuel due to the stoichiometric relationship:



The subscripts fu and ox denote the fuel and the oxidizer, respectively.

In a contrast to (22), the formula (20) holds the initial mixture stoichiometry true in the course of all stages of combustion, that is,  $dr/dt = 0$ , and product concentrations can be used to calculate the chemical equivalence ratio.

Unlike (22), the equivalence ratio defined by (20) remains unchanged at every stage of the combustion process, that is,  $dr/dt = 0$ , and so the measured or calculated product concentrations can always be used to calculate the chemical equivalence ratio. This facilitates the construction of dynamic maps, see Figures 4 and 10–13. Before constructing a map, each species in the mixture must be classified as a fuel, an oxidizer, or a species with zero valency (also known as SSPs, saturated stoichiometric products) [49]. It is important to account for the effects of SSP species that may be present in the initial mixture when determining the chemical equivalence ratio; for example, mixtures containing recirculated exhaust gases are enriched by CO<sub>2</sub> and H<sub>2</sub>O. In this way, it is able to distinguish between chemical species originated as products of the combustion process and those introduced as the EGR species.

When a cluster of cells intersects the peninsulas in which emissions (NO<sub>x</sub> or soot) are formed, it characterizes the processes that lead to their formation. Another advantage of this analytical technique is that it is possible to simultaneously obtain maps for multiple different chemical species that are involved in a process of interest. For example, in the case of NO formation, it is interesting to study oxygen molecules and atoms (O<sub>2</sub> and O) and the hydroxyl radical, OH. This facilitates the quantitative analysis of emission-forming processes.

### 3. Modeling Results and Discussion

#### 3.1. Results of the Chemical Equilibrium/Kinetics Calculation.

The predicted equilibrium adiabatic temperatures for different fuel/air mixtures are shown in Figure 5(a). For lean mixtures ( $\phi < 1.0$ ), the temperature curves for three different fuel/air mixtures coincide with one another. Under rich conditions ( $\phi > 1.0$ ), PME generates consistently lower ( $\sim 70^\circ\text{C}$ ) temperatures than DOS when  $\phi < 3.0$ . This difference increases drastically for richer mixtures ( $\phi > 3.0$ ) and reaches  $110^\circ\text{C}$  for  $\phi = 9.0$ . In a contrast, RME generates only slightly higher ( $< 10^\circ\text{C}$ ) temperatures than DOS in rich mixtures ( $\phi < 2.0$ ) and generates lower temperatures than DOS as the mixture becomes increasingly rich, reaching a maximum value of  $60^\circ\text{C}$  under the richest conditions examined.

The mole fraction of NO at equilibrium for mixtures with equivalence ratios between  $0.1 < \phi < 2.5$  is plotted in Figure 5(b). At higher equivalence ratios, the NO concentration was extremely small and is not presented. It can be seen that the peak NO concentration occurs at an equivalence ratio of 0.78 for all three fuels. Over the equivalence ratios considered, RME and DOS generate the same equilibrium concentrations of NO aside from in a very narrow range (0.75–0.80), in which RME generates a slightly higher peak value. Under the similar  $\phi$  range, the curve for PME gives slightly lower NO value and mirrors that of DOS for other  $\phi$  values. These two pictures illustrate that the temperature difference between DOS and RME is relatively modest and so cannot be responsible for the large ( $\sim 10\%$ ) increase in  $\text{NO}_x$  emissions described in the EPA report. On the other hand, RME and PME generated a lower ( $< 20^\circ\text{C}$ ) adiabatic temperature and a similar NO concentration for rich mixtures ( $1.0 < \phi < 2.0$ ). This unexpected result demonstrates that, when using PME, NO formation is not governed by thermal factor alone.

The equilibrium concentrations of methylidyne/methylene radicals (CH and  $\text{CH}_2$ ), which are essential for the initiation of prompt NO formation, are shown (as functions of the equivalence ratio) in Figures 5(c) and 5(d), respectively.

In general, DOS/air mixtures contain less CH under slightly rich ( $\phi < 1.8$ ) conditions and more CH under much richer ( $1.8 < \phi < 6.0$ ) conditions than do the corresponding RME/air mixtures. The maximum CH concentration occurs at equivalence ratios of 1.7 for both DOS and RME. With PME, the CH concentration keeps a similar value as that of DOS at the region  $\phi < 1.6$ . Above this point, the CH level deviates from DOS curve and goes underneath it.

The absolute  $\text{CH}_2$  concentration under any given set of conditions is typically about an order of magnitude greater than that of CH under the same conditions. For these three fuel/air mixtures, the  $\text{CH}_2$  concentration increases rapidly from  $\phi \approx 1.2$ , reaching a plateau that spans the region between  $\phi \approx 2.0$  and  $\phi \approx 3.0$ . Above  $\phi \approx 3.0$ , the concentration of  $\text{CH}_2$  increases further, peaking at around  $\phi \approx 3.4$ . Beyond this point, the  $\text{CH}_2$  concentration falls very slightly. The  $\text{CH}_2$  concentration curves for RME and DOS coincide in the range  $1.2 < \phi < 3$ . When  $\phi > 3$ , the  $\text{CH}_2$  concentration generated using DOS is  $\sim 25\%$  higher than that generated with RME. The  $\text{CH}_2$  concentration for PME takes the same

value as for DOS and RME under sub-stoichiometric conditions till  $\phi \approx 2.0$ . For a more rich mixture, the  $\text{CH}_2$  concentration starts to fall down from the level observed with RME. These two separate peaks in the  $\text{CH}_2$  plot are related to the formation/reduction of NO ( $\phi < 2$ ) and soot ( $\phi > 3$ ) [50]. The similar trend in CH plot is just a consequence of  $\text{CH}_2$  distribution.

By correlating these four plots, it was found that the noticeable equilibrium NO concentrations occurred in the  $0.1 < \phi < 2.0$  region, where RME and DOS afforded very similar temperatures and concentrations of CH/ $\text{CH}_2$  and NO (although the peak CH/ $\text{CH}_2$  concentration was slightly higher for RME for  $\phi \approx 1.8$ ). It was expected that since DOS and RME generated very similar adiabatic temperature profiles, they would also generate similar NO concentration profiles. However, the higher CH concentration observed with RME should favor prompt NO formation a little bit thus resulting in RME generating a higher NO concentration at rich mixture regime. As such, the fact that DOS and RME have near-identical NO emission profiles cannot be explained by considering adiabatic temperature factors and prompt NO formation alone. The nearly identical adiabatic temperature for all fuels in a full  $\phi$  range are indicative that lower LHV's for biodiesels are mostly due to fuel-bound oxygen atoms, but not a particular structure of the fuel molecules.

**3.2. PSR Modeling Results.** The normalized sensitivity coefficients for NO with respect to important reactions rate generated by PSR modeling are shown in Figure 6 for (a) DOS and (b) RME, focusing on the most sensitive reactions in the NO formation process. Three different temperatures ( $1226.84^\circ\text{C}$ ,  $1526.84^\circ\text{C}$ , and  $2026.84^\circ\text{C}$ ) were examined. A positive sensitivity coefficient, as observed for the thermal NO formation reactions, indicates that increasing temperatures accelerate the formation of NO, while negative sensitivity coefficients indicate the opposite. Reactions for which no bar is shown do not significantly affect the rate of NO formation at the indicated temperature. The plots indicate that the most sensitive reactions (of both the Zeldovich and the NCN-based prompt NO mechanisms) had significant effects on both the combustion of RME and that of DOS.

This means that NO formation is dominated by the same reactions for both RME and DOS. As shown, the prompt NO reactions (R434, R439, R449, R459, R460) are important at low-temperature,  $1226.84^\circ\text{C}$ . Their influence decreases as the temperature rises. Once the temperature reaches  $2026.84^\circ\text{C}$ , NO formation becomes governed by the Zeldovich mechanism (R336, R338). The branching reactions (R140, R141, R142) that consume the active species O and  $\text{O}_2$  compete with those involved in NO formation in both the thermal and prompt mechanisms and thus have the largest negative sensitivity coefficients.

**3.3. Diesel Engine Modeling Results.** The predicted in-cylinder parameters for the Volvo D12C diesel engine fueled by DOS and RME are plotted in Figures 7 and 8. The detailed

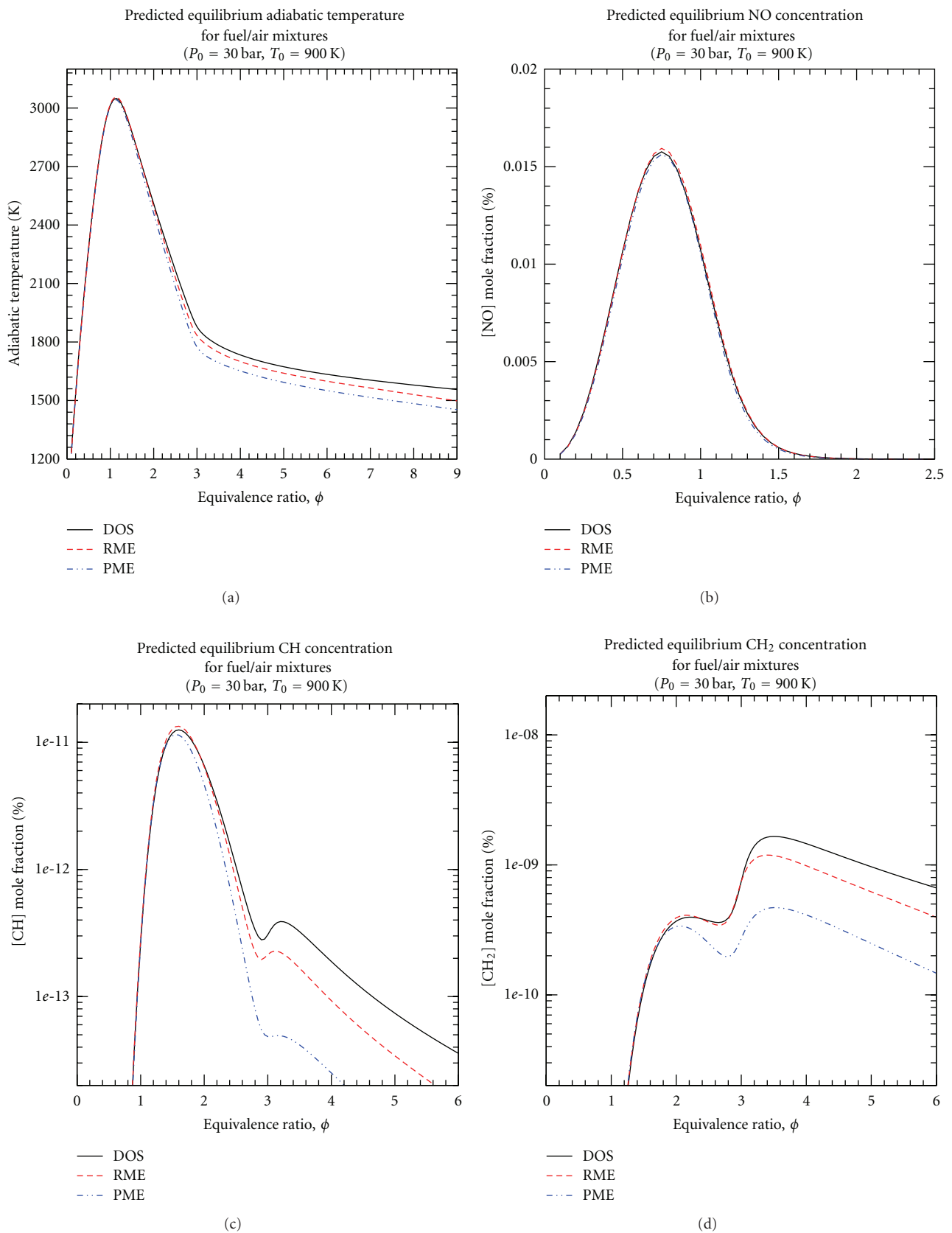


FIGURE 5: Predicted equilibrium (a) adiabatic temperature, (b) NO concentration (c) CH concentration, (d) CH<sub>2</sub> concentration for DOS/air (black line), RME/air (red dash line), and PME/air (blue dash line with dots) mixtures.  $T_0 = 626.84^\circ\text{C}$ ,  $P_0 = 3000$  kPa.

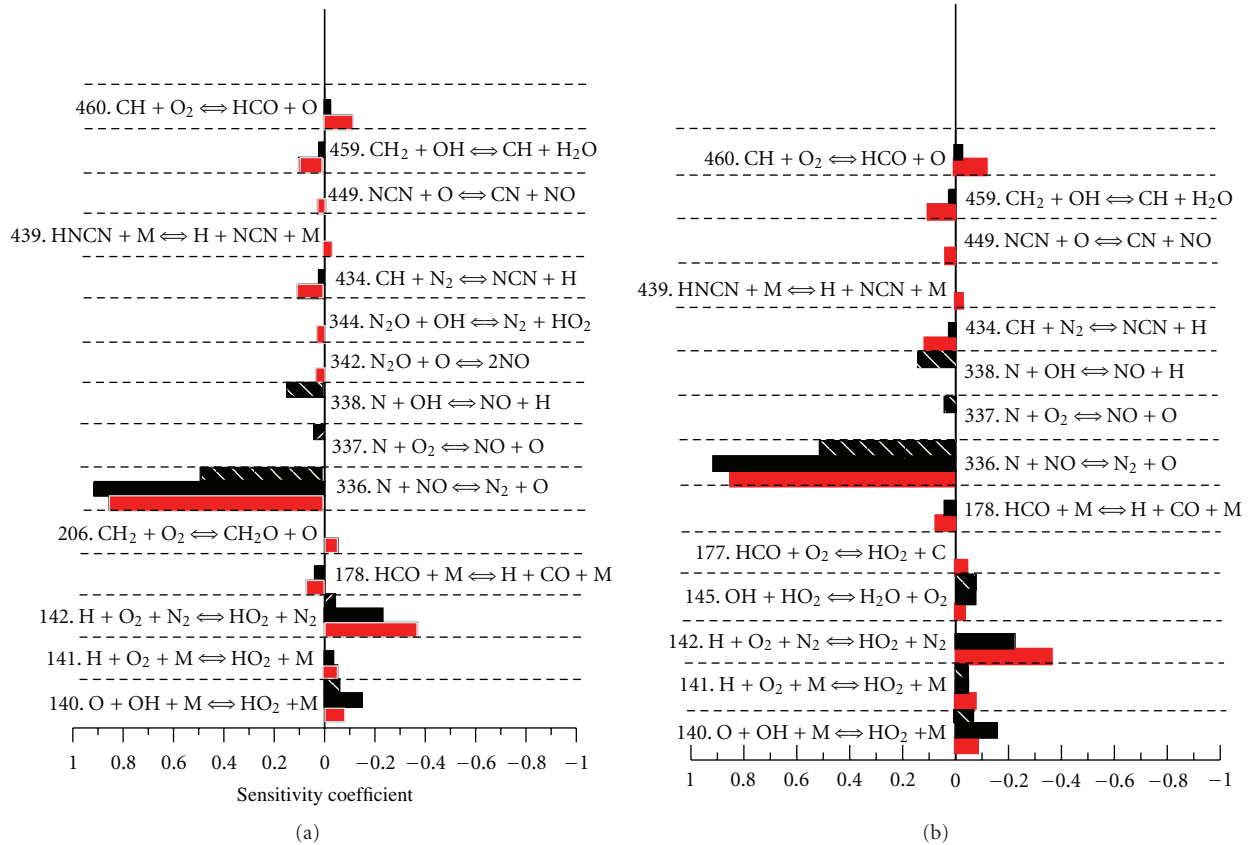


FIGURE 6: The normalized sensitivity coefficients for NO with respect to the important reaction rates, (a) DOS, (b) RME at different temperatures (red bars indicate sensitivity coefficients at 1226.84°C, black bars at 1526.84°C, and hatched bars at 2026.84°C).

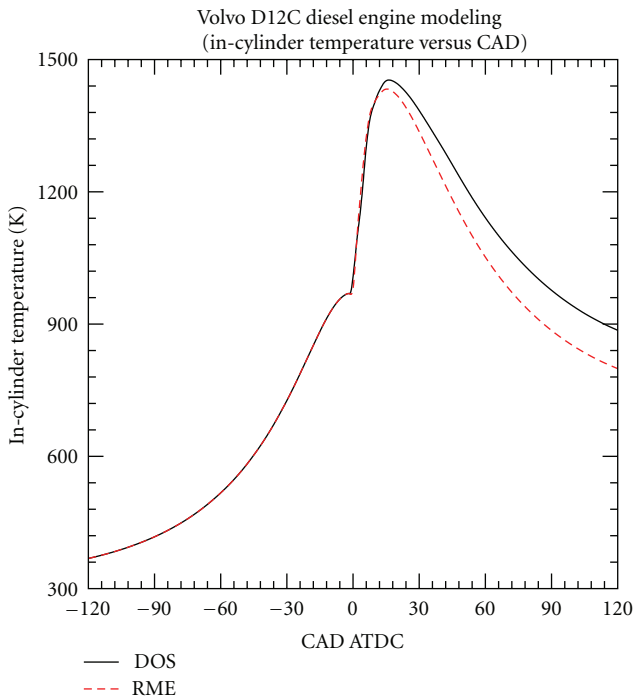


FIGURE 7: Averaged in-cylinder temperatures for the Volvo D12C diesel engine fuelled by DOS (solid line) and RME (dash line), without EGR.

PME oxidation mechanism was not used in the 3D engine simulation because of its size. Instead, the reduced mechanism based on the surrogate components was used. Since this study was focused on the formation of NO, only parameters relevant to this process (averaged in-cylinder temperature, NO concentrations) are discussed; parameters such as the in-cylinder pressure and energy release rate are ignored as illustrations even though they are important in characterizing engine performance. As shown in Figure 7, before the onset of combustion, the average in-cylinder temperature curves for DOS and RME are identical. The main combustion starts around top dead center (TDC). The heat released by the chemical reactions causes the in-cylinder temperature to increase, peaking after TDC. DOS gives a higher temperature due to its greater lower heat value (LHV), (44 MJ/Kg) compared to RME (37 MJ/Kg). This temperature difference increases during the expansion stroke.

The in-cylinder NO concentrations were plotted as functions of CAD ATDC. Both DOS and RME fuels were tested with the NCN prompt NO mechanism and without to assess the contribution of each NO formation mechanism. As shown, the NO concentration increases sharply after the initiation of combustion and remains high until combustion is complete. The NO curves explicitly show that most of the NO is formed during the early stages of combustion. The combustion temperature during the late expansion stroke does not affect the final NO concentration.

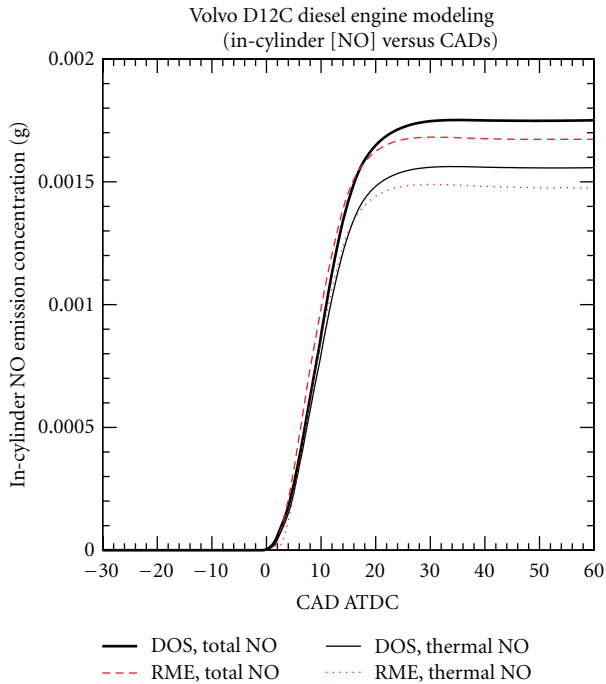


FIGURE 8: Averaged in-cylinder NO concentrations (total value indicated by bold line, thermal NO by the thin line) for the Volvo D12C diesel engine fuelled by DOS (solid line) and RME (dashed line), without EGR.

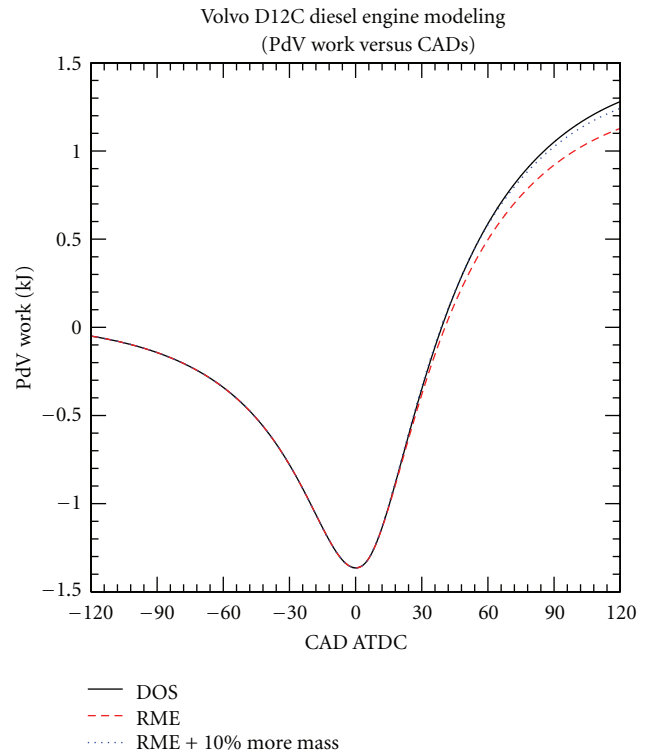


FIGURE 10: Predicted PdV work for the Volvo D12C diesel engine fuelled by DOS (black solid line), RME (red dashed line) and RME+ (dash-dot line), without EGR.

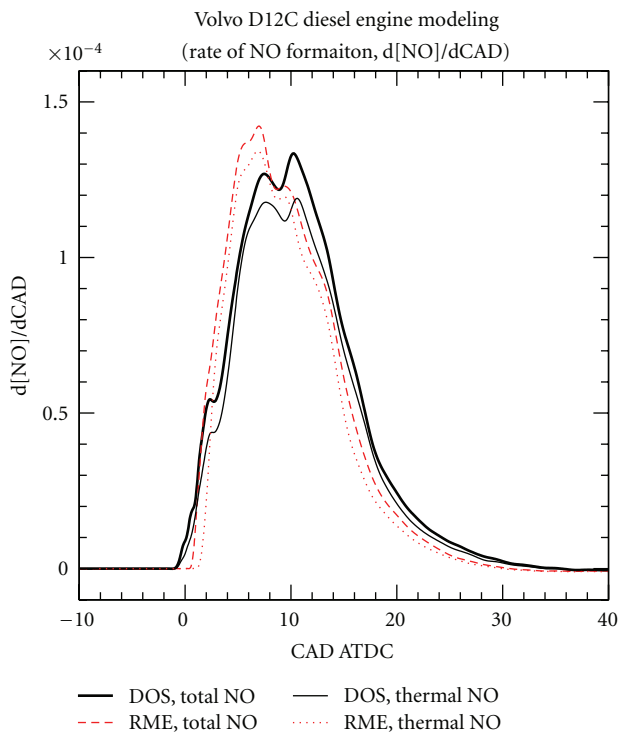


FIGURE 9: Averaged in-cylinder rates of NO formation for the Volvo D12C diesel engine fuelled by DOS (black solid line) and RME (red dashed line), without EGR.

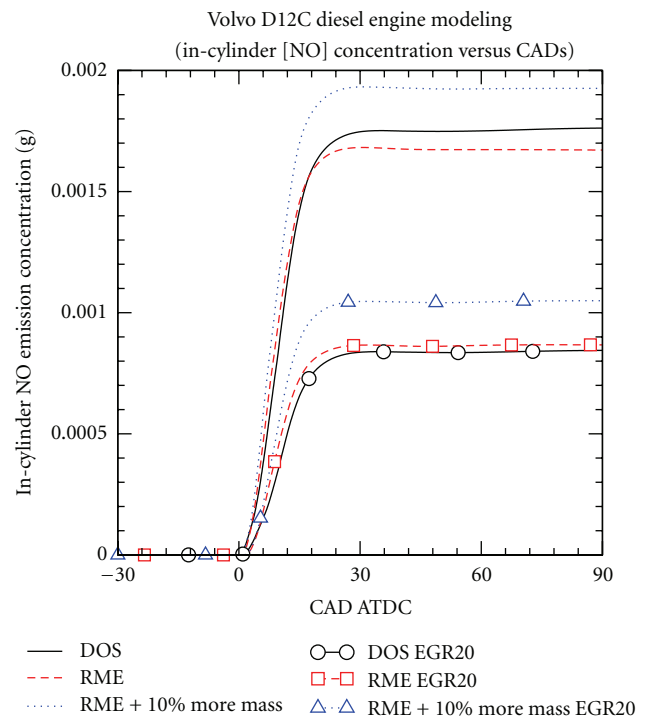


FIGURE 11: Impact of EGR level on the averaged in-cylinder NO concentrations (total value) for the Volvo D12C diesel engine fuelled by DOS (solid line), RME (dash-dot line), and RME+ (dotted line) without EGR; the same line style with symbols was the results for 20% EGR level condition.

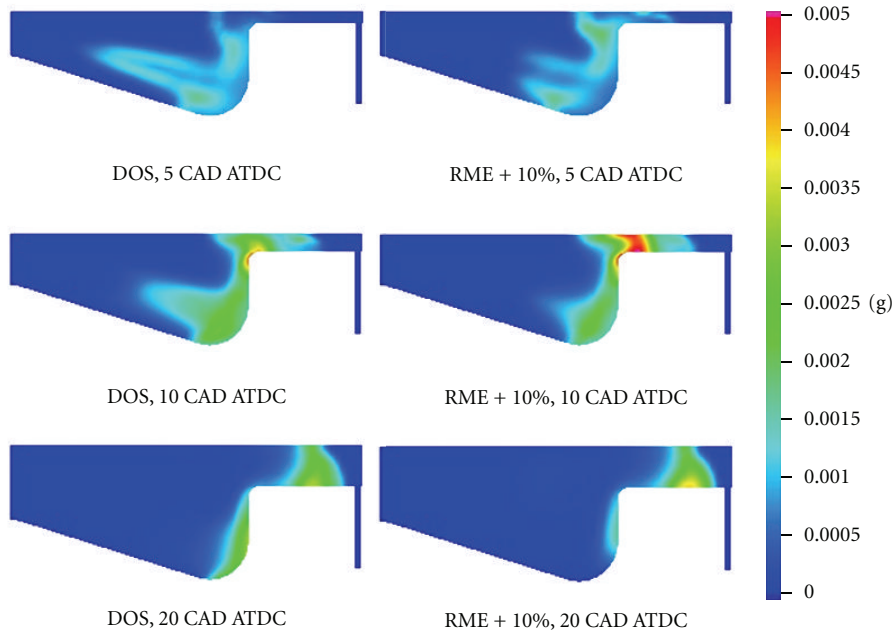


FIGURE 12: In-cylinder NO concentration distribution for the Volvo D12C diesel engine fuelled by DOS and RME+ 10% at 5, 10, 20 CAD ATDC without EGR.

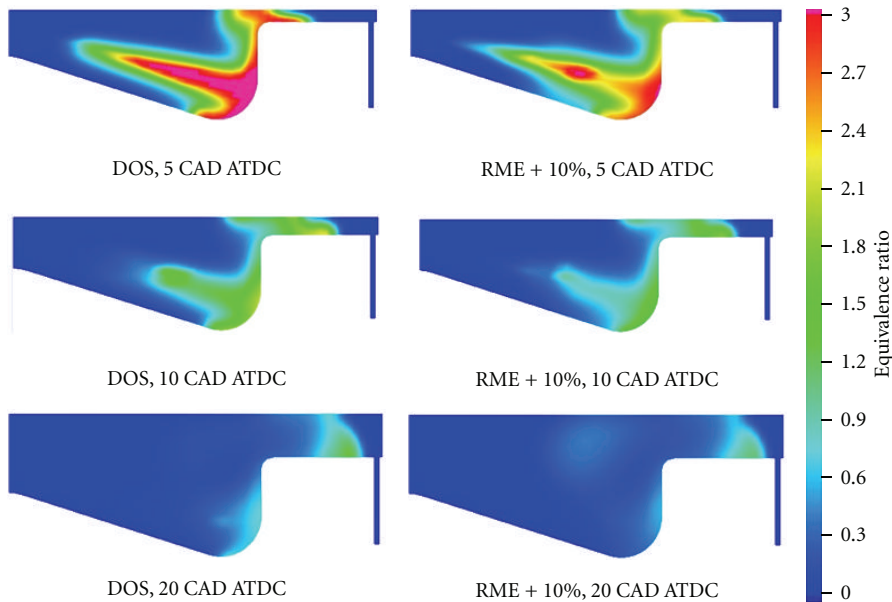


FIGURE 13: In-cylinder equivalence ratio distribution for the Volvo D12C Diesel engine fuelled by DOS and RME+ 10% at 5, 10, 20 CAD ATDC without EGR.

The peculiarities of NO formation are illustrated by the data on the rate of NO formation shown in Figure 9. It is observed that when using RME, the rate of NO formation begins to rise at a later stage than is the case of DOS. But once the NO formation was initiated, it goes beyond that of DOS immediately.

To compensate the reduced energy content of biodiesel fuel, extra RME ( $67 \times 10^{-6}$  kg, which is 10% more in mass relative to the original value), called RME+, was injected

into the engine cylinder, that, on the other hand, keeps the engine operating on a constant power delivery basis. In general, the indicated engine work is represented by the pressure-volume work, or PV work, which is the integration of differential component PdV work on the CADs. Hence, by comparing the PdV work, one can examine if the combustion of different fuels gives the same indicated engine work (see Figure 10), in other words, a constant power delivery. Figure 10 illustrates that RME combustion (dot/dash line)

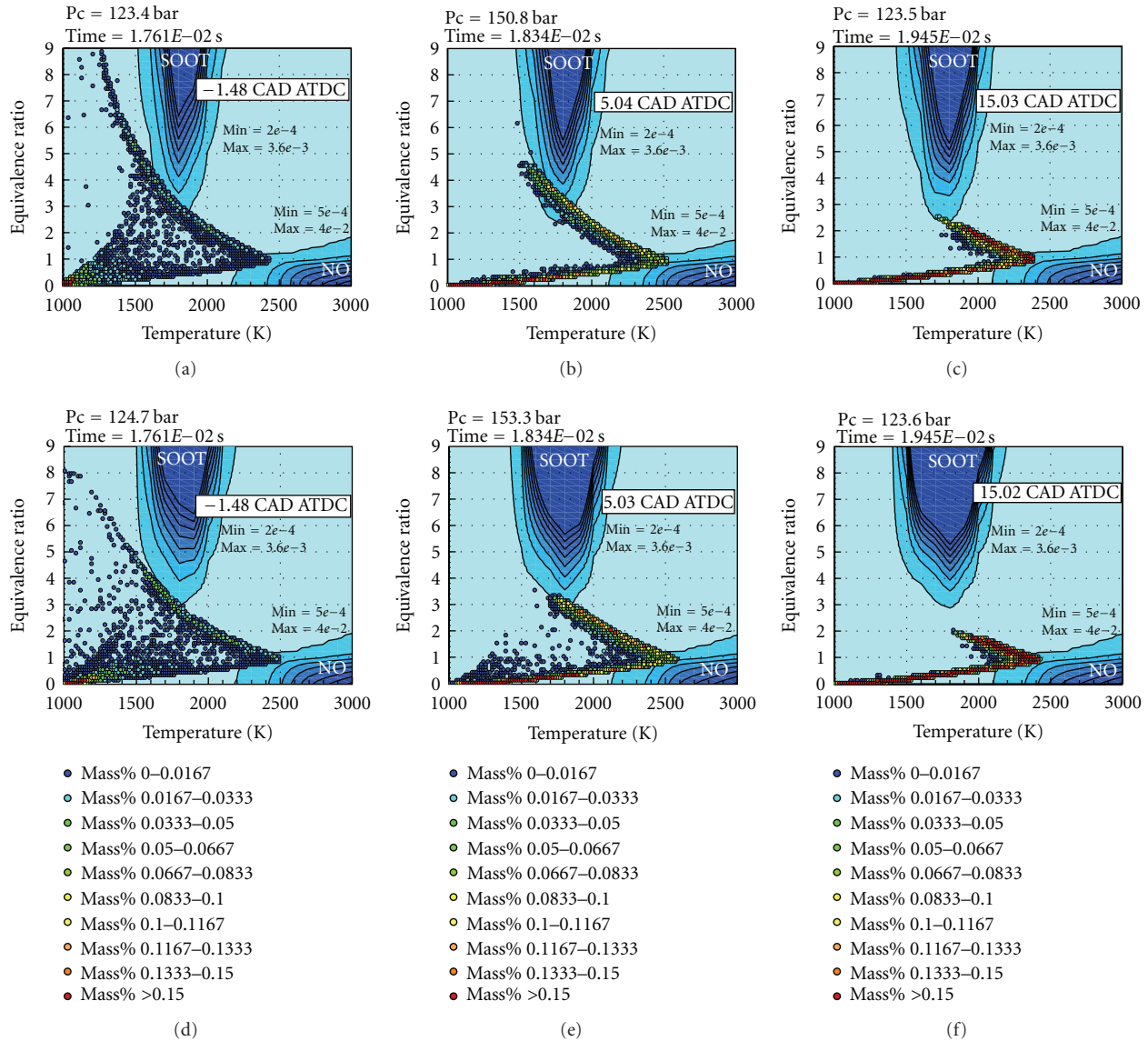


FIGURE 14: Parametric  $\phi$ - $T$  emission maps for instant soot and NO concentrations in the Volvo D12C Diesel engine fuelled by DOS (a–c) and RME (d–f) at different CADs (–1.5, 5.0, and 15.0, resp.); the engine was operated under 50% load with 30% EGR.

gives identical PdV value as diesel oil combustion (solid line) at the compression stroke, slightly lower PdV value at the expansion stroke. The RME+ produces exactly the same PdV value as diesel oil during the whole calculating engine cycle.

The predicted total in-cylinder NO concentration of the Volvo D12C diesel engine fuelled by diesel oil, RME, and RME+ was presented in Figure 11 for two different EGR levels: 0% and 20%. It shows the RME+ produce more NO emission compared to the pure diesel oil. This was observed for both EGR levels and represented the emission trends under the real engine operating conditions. Aside from this, one can also conclude that the cooling impact of EGR on the reduction of NO emission is more noticeable for the combustion of diesel oil, since the difference of NO value between 0% EGR (solid line) and 20% EGR (solid line

sampled by circles) is larger than that of RME. Such a less-effective EGR behavior of RME fuel is ascribed that the fuel-bound oxygen in RME fuel molecular (approx. 11% in mass fraction) and the additional oxygen in the EGR gas following biodiesel combustion results in less inert species ( $\text{CO}_2$ ,  $\text{H}_2\text{O}$ , etc.) which are present to absorb the heat of combustion, hence less cooling effect [16].

The final absolute NO concentrations for the combustion of these three fuels under two different EGR levels are shown in Table 6. As shown in Table 6, for 0% EGR level, the prompt NCN pathway accounts for 11.1% and 12.1% of the NO formation with DOS and RME, respectively. These data demonstrate that the prompt NO mechanism cannot explain the increased  $\text{NO}_x$  emissions described in the EPA report, since the mechanism is relevant in both RME

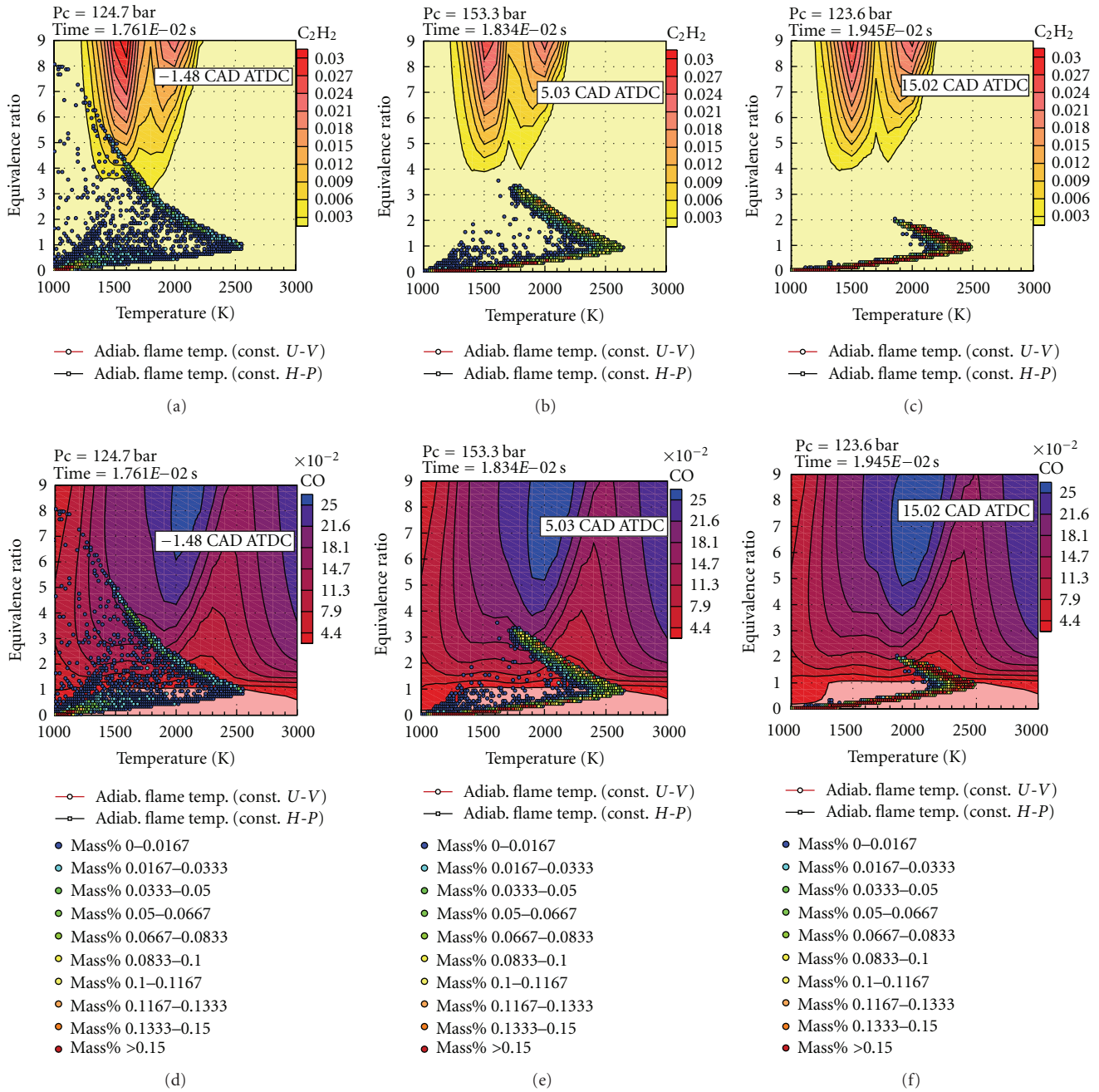


FIGURE 15: Parametric  $\phi$ - $T$  emission maps for instant acetylene,  $C_2H_2$  concentrations (upper three plots) and carbon monoxide, CO concentrations (a, b, and c) in the Volvo D12C Diesel engine fuelled by RME at different CADs (-1.5, 5.0 and 15.0, resp.); the engine was operated under 50% load with 30% EGR.

and diesel combustion. Moreover, the contribution of the thermal NO mechanism is also similar for RME and DOS. However, for RME+, the thermal NO was promoted ~4% and the prompt NO was suppressed ~4% in proportion. The total NO increases ~10% compared with that of diesel oil combustion. This modeling result corroborated the similar emission trend reported by EPA.

Once a 20% EGR level was charged for the Volvo D12C diesel engine, the thermal NO formation is drastically reduced more than 50% for all fuels due to the suppressing

effect of lower-temperature combustion. The prompt NO emission for diesel oil and RME decreased only slightly but is kept nearly constant for RME+. Thereby, the proportion of prompt NO in the total NO concentration goes up generally for all fuels with EGR conditions.

To achieve deeper insights for the biodiesel  $NO_x$  increases, the in-cylinder NO concentration contour was visualized at difference crank angle instants for diesel oil and RME+, see Figure 12. One can see that the NO is mainly formed around the periphery of the reacting mixture. RME+

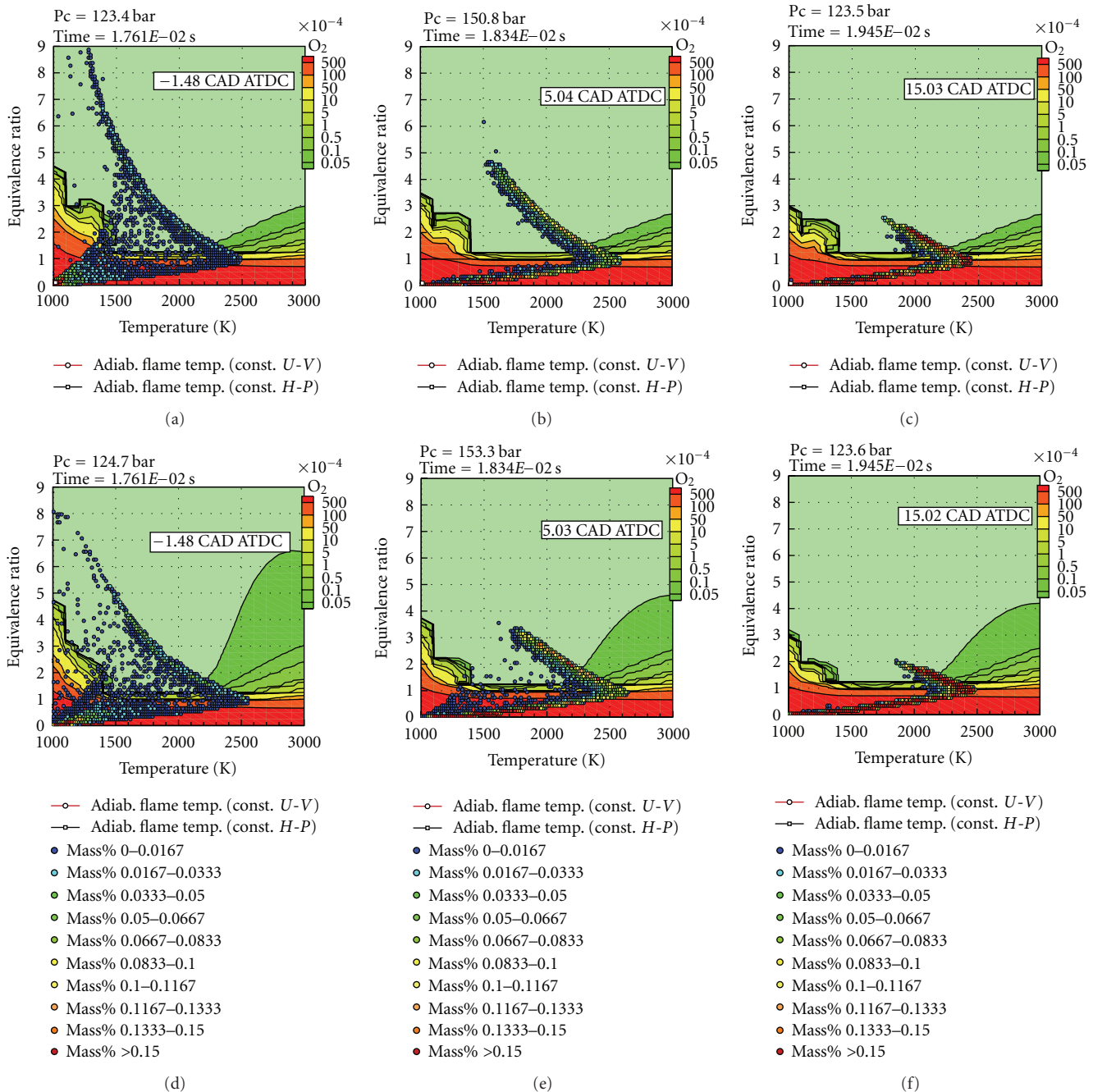


FIGURE 16: Parametric  $\phi$ - $T$  maps for instant  $O_2$  concentrations in the Volvo D12C Diesel engine fuelled by DOS (a, b, and c) and RME (d, e, and f) at different CADs (-1.5, 5.0, and 15.0, resp.); the engine was operated under 50% load with 30% EGR.

combustion has a much wider and deeper colored (red and yellow) region around the periphery of the reacting mixing compared to diesel oil combustion, which means more NO was formed at this region.

**3.4.  $\phi$ - $T$  Parametric Maps.** Thus, neither the chemical equilibrium/kinetics calculations nor the 3D engine modeling provided any evident clues as to the origin of the increased  $NO_x$  emissions observed when using biodiesel. However, Figure 5(b) shows that  $NO$  is formed in a rather narrow

equivalence ratio range. As such, a small variation in  $\phi$  could have a significant effect on the  $NO$  concentration. If combustion with RME will typically occur under leaner conditions than is the case with DOS, say with a 10% smaller value of  $\phi$ , the quantity of  $NO$  formed during the combustion of RME would be  $\sim 15\%$  greater than that formed with DOS, assuming that, in both cases, combustion was to proceed with an equivalence ratio between 0.78 and 1.5. This alone could, in principle, explain why biodiesel produces more  $NO_x$  during combustion. To verify if biodiesel

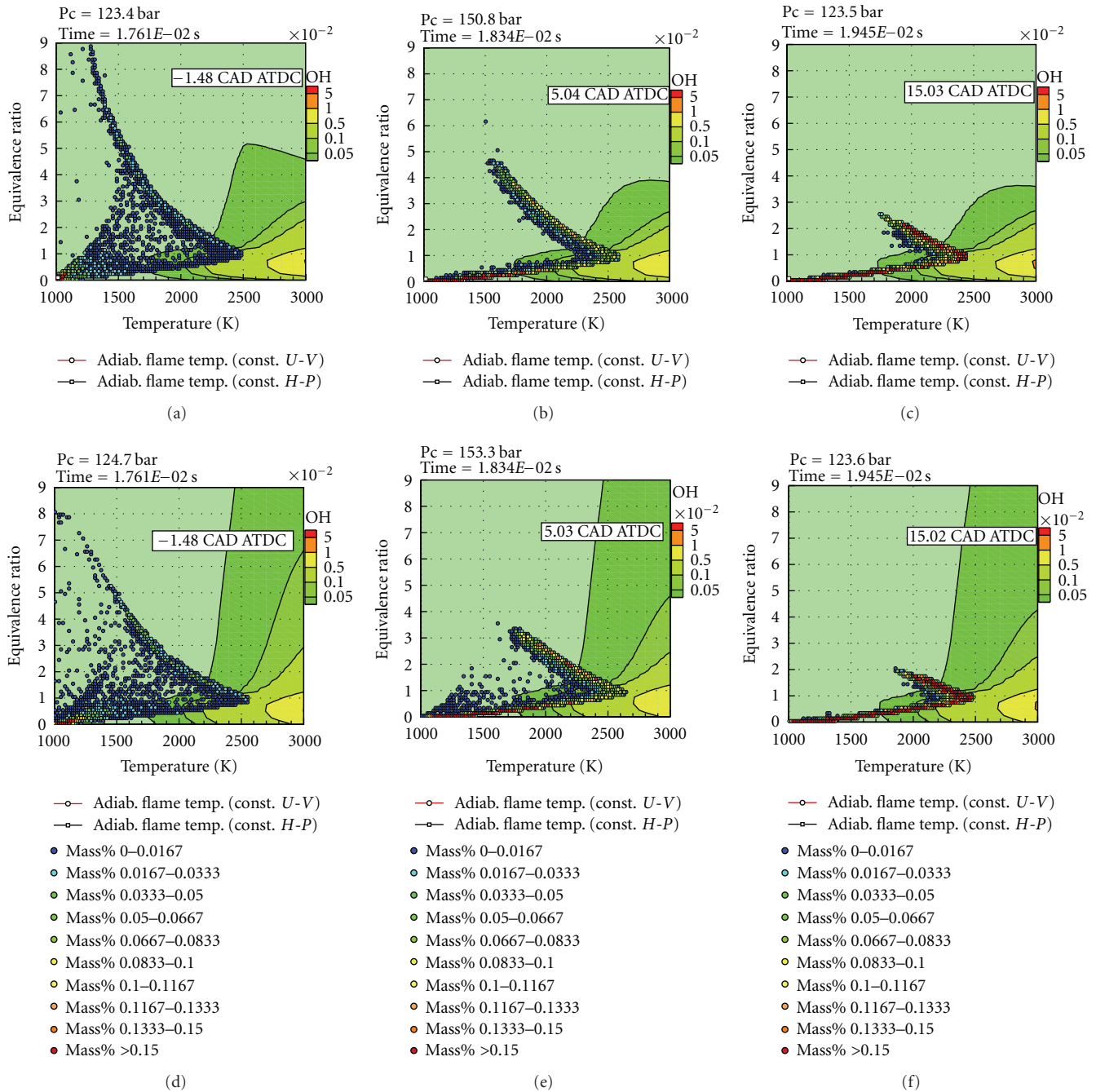


FIGURE 17: Parametric  $\phi$ - $T$  maps for instant OH concentrations in the Volvo D12C Diesel engine fuelled by DOS (a, b, and c) and RME (d, e, and f) at different CADs (-1.5, 5.0, and 15.0, resp.); the engine was operated under 50% load with 30% EGR.

combustion really has a leaner combustion, the equivalence ratio distribution in the diesel engine cylinder was presented for both diesel oil and RME at the same CADs instants as Figure 12, see Figure 13.

One can overlap the NO contour and equivalence contour and find out the highest NO concentration region locates at  $\phi(0.6 \sim 1.8)$  under the diesel engine operating conditions. For the too high (red color) or too low (blue) equivalence ratio region, there is no NO formed (colored by blue) in Figure 12.

Furthermore, a convincing proof would be required to support the above conjecture. Such proof was obtained by analysis of dynamic  $\phi$ - $T$  maps for relevant in-cylinder species NO, O, and OH. The maps provide explicit visualizations of the conditions under which NO was formed and the distributions of the relevant species. The maps presented in Figures 14–17 were constructed for the Volvo D12C engine fuelled by DOS and RME operating under 50% load with 30% EGR, at the same indicated engine work for the tested fuels. Under these conditions, increased biodiesel  $\text{NO}_x$

TABLE 6: The absolute NO concentration values contributed by different mechanisms for DOS, RME, and RME+ under 0% and 20% EGR level conditions.

Fuel	NO			
	Thermal NO ppm	Prompt NO ppm	Total NO ppm	Proportion % : %
DOS	551.0	68.6	619.6	88.9 : 11.1
RME	516.0	71.0	587.0	87.9 : 12.1
RME+ 10% more mass	617.49	57.86	675.35	91.4 : 8.6
DOS EGR20	244.32	52.58	296.9	82.3 : 17.7
RME EGR20	251.05	52.95	304.0	82.6 : 17.4
RME+ 10% mass EGR20	309.0	58.91	367.91	86.0 : 14.0

emissions consistent with the EPA report were observed in both experiments and simulations [11].

Figure 14 illustrates the instantaneous abundance of two in-cylinder species, soot and NO, for DOS and RME at different crank angles. It shows that NO formation occurs with relatively lean mixtures ( $\phi < 2.0$ ) at high temperatures ( $1927^\circ\text{C} < T < 2727^\circ\text{C}$ ), while soot was formed in rich mixtures ( $\phi > 3$ ) at moderate temperatures ( $1227^\circ\text{C} < T < 1727^\circ\text{C}$ ). These emission formation trends are not fuel specific, but by comparing Figures 14(a)–14(c) with 14(d)–14(f), it is apparent that, for RME combustion, the soot peninsula extends further in both the low- ( $<1227^\circ\text{C}$ ) and high- ( $>1727^\circ\text{C}$ ) temperature directions. That is to say, when using RME, soot formation occurs under a wider range of temperatures; in DOS combustion, these temperatures are either too low to allow soot formation or so high as to oxidize the soot as it forms. However, under these conditions, the area of intersection between the cluster points and the soot peninsula is narrower for RME (see Figures 14(d) and 14(f)) than for DOS (see Figures 14(a) and 14(c)), which is consistent with the observation that less soot is formed during RME combustion. Quantitative data on these processes can be obtained from the results of the 3D engine modeling.

The other intermediates, acetylene,  $\text{C}_2\text{H}_2$  as a major soot precursor, and carbon monoxide, CO, for RME, are presented in Figure 15 to illustrate soot formation at incomplete combustion conditions. However, soot formation and oxidation are not the primary focus of this work, and they are not discussed further herein.

In terms of the formation of NO, the cell points show that for RME, the gaseous mass intersecting the NO formation region is larger than for DOS, in terms of both size (compare Figures 14(b) and 14(d)) and cell mass (compare the red areas in Figures 14(c) and 14(f)). This means that more NO is produced in the instant captured in the plots with RME than with DOS. The hypothesis that the leaner combustion that occurs when using biodiesel is responsible for the observed increase in NO emissions can be evaluated by constructing maps for the oxygen molecules or other oxidizing species at different crank angles. Because the equivalence ratio is determined by the  $\text{O}_2$  concentration in the air and in the structure of the fuel molecules, it is interesting to study the effect of fuel-bound oxygen atoms on NO formation.

The  $\phi$ - $T$   $\text{O}_2$  species maps at different CADs are shown in Figure 16 for DOS (upper three plots) and RME (lower three plots). The different colors indicate the concentration of  $\text{O}_2$ , with red denoting the highest concentrations, yellow denoting the intermediate value, and green denoting low concentrations. At temperatures between  $1226.84^\circ\text{C}$  and  $2726.84^\circ\text{C}$ , the highest  $\text{O}_2$  level occurs under very lean conditions. A transition from the highest concentration to the lowest occurs within a narrow  $\phi \approx 1$  region. One can see that a small amount of  $\text{O}_2$  is observed even for the rich mixtures ( $\phi \approx 3$ ). However, the green color occupies a very narrow area. This may be due to the fact that combustion requires the temperature to be sufficiently high to overcome the activation barriers of the reactions that initiate combustion. Under low-temperature conditions, the low rate of fuel oxidation means that more  $\text{O}_2$  is available. Once again, the  $\text{O}_2$  contour is not fuel specific.

It is apparent that, in RME combustion, more  $\text{O}_2$  is present in the high temperature region ( $T > 1726.84^\circ\text{C}$ ); see the green regions in the lower three plots of Figure 16. This is because RME is an oxygenated fuel that requires less external  $\text{O}_2$  in order for combustion to occur. In the low-temperature range ( $T < 1726.84^\circ\text{C}$ ), slightly less  $\text{O}_2$  was retained with RME than with DOS due to its lower oxidation threshold. NO species are formed by the reaction of molecular nitrogen with oxidizing species at high temperatures; when using RME, the amount of available  $\text{O}_2$  at these high temperatures with equivalence ratios between 0 and 5 is noticeably greater than is the case with DOS. As such, the fact that RME undergoes relatively lean combustion because of its oxygen content may explain increased NO emissions shown in Figure 14.

The hydroxyl (OH) radical also plays a significant role in thermal NO formation; maps for this species are shown in Figure 17. The same colors as were used previously are used to indicate the OH concentrations. It was observed that more OH radicals are formed during RME combustion, as shown by the greater width of the yellow regions in lower three plots of Figure 17. However, as discussed above, thermal NO formation alone cannot fully account for the increased  $\text{NO}_x$  emissions observed with biodiesel.

The approach developed herein also forecasts that the short-chain biodiesel, for example, mb, with a relatively

higher oxygen content can form too lean combusting mixture ( $\phi < 0.78$ ) and produce less  $\text{NO}_x$  emissions.

#### 4. Conclusion

Chemical equilibrium and kinetics calculations show that similar flame temperatures are achieved with RME and DOS, giving rise to comparable NO mole fractions under equilibrium conditions. The adiabatic temperature was predicted to be lower when using PME, but the NO concentrations generated using this fuel were nevertheless similar to those predicted for the other two over a wide range of equivalence ratios. In terms of the species involved in the formation of NO, it was predicted at low and moderate equivalence ratios ( $\phi < 1.6$ ). RME/air mixtures have the coincident equilibrium concentrations of the CH radical, but for richer mixtures, the CH radical is more abundant in DOS/air mixtures. Only at a very narrow region ( $1.6 < \phi < 2$ ), a slightly higher CH concentration was observed for RME/air mixture. Both DOS and RME generate similar concentrations of  $\text{CH}_2$  at equivalence ratios that most strongly favor the formation of NO ( $\phi < 3.0$ ). Under lean conditions, the levels of CH and  $\text{CH}_2$  generated using PME are similar to those observed with DOS, but with rich mixtures, PME generates far fewer of these radicals. Sensitivity analysis showed that both the thermal and the prompt NO mechanisms are involved in the formation of NO during the combustion of DOS and RME, and that the thermal mechanism is dominant.

Diesel engine modeling was established for DOS, RME and RME+ for both without and with 20% EGR levels. Without EGR the thermal and prompt NO formation mechanisms account for approximately ~89% and ~11% of the total NO produced, respectively. The 20% EGR level could cause more than 50% reduction of thermal NO, but less pronounced effects on the prompt NO formation. Consequently, the increased NO emissions generated by the combustion of biodiesel cannot be attributed to a greater importance of the prompt mechanism. It was also observed that RME+ produces 10% more NO than DOS for both EGR levels. Aside from this, the cooling effect of EGR on the thermal NO reduction is less effective for RME combustion than DOS due to the less inert species in the EGR composition. The 3D CFD modeling results also illustrate that most NO was formed at the region whose equivalence ratio range  $0.6 \sim 1.8$ , and the RME combustion presents a leaner combusting condition relative to that of diesel oil.

Analysis of  $\phi$ - $T$  maps demonstrated that more  $\text{O}_2$  molecules is available during RME combustion than was the case with DOS due to the presence of oxygen atoms within the RME molecules. Consequently, less external oxygen is required for combustion with RME, and RME combustion occurs under comparatively lean conditions, which favor NO formation when combustion occurs under conditions corresponding to the right-hand side of the NO- $\phi$  correlation curve.

In light of these data, it was proposed that the increased NO emissions observed when using biodiesel in conventional diesel engines are attributable to combustion effectively

occurring under leaner conditions when using oxygen-containing fuels. To test this hypothesis more rigorously, it will be necessary to conduct experiments aimed at analyzing the spatial distribution of the equivalence ratio within the cylinder of a diesel engine.

#### Acknowledgments

The support of the Engine Research Center, CERC, for Chalmers University of Technology and help of the Spanish Ministry of Science and Research for Universidad Politécnic de Valencia are gratefully acknowledged.

#### References

- [1] The US Environmental Protection Agency, "A comprehensive analysis of biodiesel impacts on exhaust emissions," Tech. Rep. EPA420-P-02001, 2002.
- [2] C. J. Mueller, A. L. Boehman, and G. C. Martin, "An experimental investigation of the origin of increased  $\text{NO}_x$  emissions when fueling a heavy-duty compression-ignition engine with soy biodiesel," SAE Paper 2009-01-1792, 2009.
- [3] W. A. Eckerle, E. J. Lyford-Pike, D. Stanton, J. Wall, L. La-Pointe, and S. Whitacre, "Effects of methyl-ester biodiesel blends on  $\text{NO}_x$  production," SAE Paper 2008-01-0078, 2008.
- [4] S. K. Jha, S. Fernando, and S. D. F. To, "Flame temperature analysis of biodiesel blends and components," *Fuel*, vol. 87, no. 10-11, pp. 1982-1988, 2008.
- [5] G. A. Ban-Weiss, J. Y. Chen, B. A. Buchholz, and R. W. Dibble, "A numerical investigation into the anomalous slight  $\text{NO}_x$  increase when burning biodiesel; A new (old) theory," *Fuel Processing Technology*, vol. 88, no. 7, pp. 659-667, 2007.
- [6] A. L. Boehman, D. Morris, J. Szybist, and E. Esen, "The impact of the bulk modulus of diesel fuels on fuel injection timing," *Energy & Fuels*, vol. 18, no. 6, pp. 1877-1882, 2004.
- [7] P. Ye and A. L. Boehman, "Investigation of the impact of engine injection strategy on the biodiesel  $\text{NO}_x$  effect with a common-rail turbocharged direct injection diesel engine," *Energy & Fuels*, vol. 24, no. 8, pp. 4215-4225, 2010.
- [8] W. C. Reynolds, *Element Potential Method for Chemical Equilibrium Analysis: Implementation in the Interactive Program STANJAN*, Department of Mechanical Engineering, Stanford University, 1986.
- [9] P. Glarborg, J. F. Grcar, and J. A. Miller, "PSR: a fortran program for modeling well-stirred reactors," Gov Pub SAND86-8209, 1992.
- [10] J. Gustavsson and V. I. Golovitchev, "Spray combustion simulation based on detailed chemistry approach for diesel fuel surrogate model," SAE Paper 2003-01-1848, 2003.
- [11] V. I. Golovitchev and J. Yang, "Construction of combustion models for rapeseed methyl ester bio-diesel fuel for internal combustion engine applications," *Biotechnology Advances*, vol. 27, no. 5, pp. 641-655, 2009.
- [12] D. L. Baulch, C. J. Cobos, R. A. Cox et al., "Summary table of evaluated kinetic data for combustion modeling," *Combustion and Flame*, vol. 98, no. 1-2, pp. 59-79, 1994.
- [13] A. A. Konnov, "Implementation of the NCN pathway of prompt-NO formation in the detailed reaction mechanism," *Combustion and Flame*, vol. 156, no. 11, pp. 2093-2115, 2009.
- [14] A. A. Amsden, "KIVA-3V: a block-structured KIVA program for engines with vertical or canted valves," Tech. Rep. LA-13313-MS, Los Alamos, NM, USA, 1997.

- [15] J. C. Beale and R. D. Reitz, "Modeling spray atomization with the Kelvin-Helmholtz/Rayleigh-Taylor hybrid model," *Atomization and Sprays*, vol. 9, no. 6, pp. 623–650, 1999.
- [16] G. Adi, C. Hall, D. Snyder et al., "Soy-biodiesel impact on NO<sub>x</sub> emissions and fuel economy for diffusion-dominated combustion in a turbo—diesel engine incorporating exhaust gas recirculation and common rail fuel injection," *Energy & Fuels*, vol. 23, no. 12, pp. 5821–5829, 2009.
- [17] M. J. Holst, *Notes on The KIVA-II Software and Chemically Reactive Fluid Mechanics*, Lawrence Livermore National Laboratory, 1992.
- [18] V. I. Golovitchev, N. Nordin, R. Jarnicki, and J. Chomiak, "3-D diesel spray simulation using new detailed chemistry turbulent combustion model," SAE Paper 2000-01-1891, 2000.
- [19] R. O. Fox, "On the relationship between Lagrangian micro-mixing models and computational fluid dynamics," *Chemical Engineering and Processing: Process Intensification*, vol. 37, no. 6, pp. 521–535, 1998.
- [20] U. Frisch, *Turbulence*, Cambridge University Press, Cambridge, UK, 1995.
- [21] V. I. Golovitchev, K. Atarashiya, K. Tanaka, and S. Yamada, "Towards universal EDC-based combustion model for compression ignition engine simulation," SAE Paper 2003-01-1849, 2003.
- [22] S. C. Kong, C. D. Marriott, C. J. Rutland, and R. D. Reitz, "Experiments and CFD modeling of direct injection gasoline HCCI engine combustion," SAE Paper 2002-01-1925, 2002.
- [23] D. Veynante and L. Vervisch, "Turbulent combustion modeling," *Progress in Energy and Combustion Science*, vol. 28, no. 3, pp. 193–266, 2002.
- [24] S. M. Aceves, D. L. Flowers, J.-Y. Cheng, and A. Babajimopoulos, "Fast prediction of HCCI combustion with an artificial neural network linked to a fluid mechanics code," SAE Paper 2006-01-3298, 2006.
- [25] <ftp://ftp.technion.ac.il/pub/supported/aetdd/thermodynamics/BURCAT.THR>.
- [26] J. A. Miller and C. T. Bowman, "Mechanism and modeling of nitrogen chemistry in combustion," *Progress in Energy and Combustion Science*, vol. 15, no. 4, pp. 287–338, 1989.
- [27] Y. B. Zeldovich, P. Y. Sadvonnikov, and D. A. Frank-Kamenetskii, *Oxidation of Nitrogen in Combustion*, Academy of Sciences of the USSR, Moscow, Russia, 1947.
- [28] Y. B. Zeldovich, G. I. Barenblatt, V. B. Librovich, and G. M. Makhviladze, *The Mathematical Theory of Combustion and Explosion*, Consultants Bureau, New York, NY, USA, 1985.
- [29] J. Wolfrum, "Bildung von stickstoffoxiden bei der verbrennung," *Chemie-Ingenieur-Technik*, vol. 44, no. 10, pp. 656–659, 1972.
- [30] J. Warnatz, U. Maas, and R. W. Dibble, *Combustion. Physical and Chemical Fundamentals, Modeling and Simulation, Experiments, Pollutant Formation*, Springer, 4th edition, 2006.
- [31] J. Tomeczek and B. Gradon, "The role of nitrous oxide in the mechanism of thermal nitric oxide formation within flame temperature range," *Combustion Science and Technology*, vol. 125, pp. 159–180, 1997.
- [32] J. Tomeczek and B. Gradoń, "The role of N<sub>2</sub>O and NNH in the formation of NO via HCN in hydrocarbon flames," *Combustion and Flame*, vol. 133, no. 3, pp. 311–322, 2003.
- [33] A. A. Konnov and I. V. Dyakov, "Nitrous oxide conversion in laminar premixed flames of CH<sub>4</sub> + O<sub>2</sub> + Ar," *Proceedings of the Combustion Institute*, vol. 32, no. 1, pp. 319–326, 2009.
- [34] C. P. Fenimore, "Studies of fuel-nitrogen species in rich flame gases," in *Proceedings of the 17th Symposium (International) on Combustion*, pp. 661–670, The Combustion Institute, Pittsburgh, Pa, USA, 1979.
- [35] G. P. Smith, "Evidence of NCN as a flame intermediate for prompt NO," *Chemical Physics Letters*, vol. 367, no. 5-6, pp. 541–548, 2003.
- [36] L. V. Moskaleva and M. C. Lin, "The spin-conserved reaction CH + N<sub>2</sub> → H + NCN: a major pathway to prompt NO studied by quantum/statistical theory calculations and kinetic modeling of rate constant," *Symposium (International) on Combustion*, vol. 28, no. 2, pp. 2393–2402, 2000.
- [37] B. A. Williams and J. W. Fleming, "Experimental and modeling study of NO formation in 10 torr methane and propane flames: evidence for additional prompt-NO precursors," *Proceedings of the Combustion Institute*, vol. 31, no. 1, pp. 1109–1117, 2007.
- [38] B. A. Williams, J. A. Sutton, and J. W. Fleming, "The role of methylene in prompt NO formation," *Proceedings of the Combustion Institute*, vol. 32, no. 1, pp. 343–350, 2009.
- [39] J. W. Bozzelli and A. M. Dean, "O + NNH: a possible new route for NO<sub>x</sub> formation in flames," *International Journal of Chemical Kinetics*, vol. 27, p. 1097, 1995.
- [40] A. A. Konnov and J. D. Ruych, "A possible new route forming NO via N<sub>2</sub>H<sub>3</sub>," in *Proceedings of the 28th Symposium (International) on Combustion*, Edinburgh, UK, 2000.
- [41] P. A. Glaude, O. Herbinet, S. Bax, J. Biet, V. Warth, and F. Battin-Leclerc, "Modeling of the oxidation of methyl esters—Validation for methyl hexanoate, methyl heptanoate, and methyl decanoate in a jet-stirred reactor," *Combustion and Flame*, vol. 157, no. 11, pp. 2035–2050, 2010.
- [42] J. L. Brakora, Y. Ra, R. D. Reitz, M. Joanna, and C. D. Stuart, "Development and validation of a reduced reaction mechanism for biodiesel-fueled engine simulations," SAE Paper 2008-01-1378, 2008.
- [43] O. Herbinet, W. J. Pitz, and C. K. Westbrook, "Detailed chemical kinetic oxidation mechanism for a biodiesel surrogate," *Combustion and Flame*, vol. 154, no. 3, pp. 507–528, 2008.
- [44] T. E. Daubert and R. P. Danner, "Physical and Thermodynamic Properties of Pure Chemicals," Part 4, 1989.
- [45] F. Battin-Leclerc, R. Bounaceur, G. M. Côme et al., *EXGAS-Alkanes, A Software for the Automatic Generation of Mechanisms for the Oxidation of Alkanes*, User Guide, Cedex, France, 2004.
- [46] K. Akihama, Y. Takatori, K. Inagaki, S. Sasaki, and A. M. Dean, "Mechanism of the smokeless rich diesel combustion by reducing temperature," SAE Paper 2001-01-0655, 2001.
- [47] V. I. Golovitchev, A. T. Calik, and L. Montorsi, "Analysis of combustion regimes in compression ignited engines using parametric  $\phi$ -T dynamic maps," SAE Paper 2007-01-1838, 2007.
- [48] A. E. Lutz, R. J. Kee, and J. A. Miller, "SENKIN: a fortran program for predicting homogeneous gas phase chemical kinetics with sensitivity analysis," Sandia Report SAND87-8248, 1994.
- [49] C. J. Mueller, "The quantification of mixture stoichiometry when fuel molecules contain oxidizer elements or oxidizer molecules contain fuel elements," SAE Paper 2005-01-3705, 2005.
- [50] S. Cheskis, I. Derzy, V. A. Lozovsky, A. Kachanov, and F. Stoeckel, "Intracavity laser absorption spectroscopy detection of singlet CH<sub>2</sub> radicals in hydrocarbon flames," *Chemical Physics Letters*, vol. 277, no. 5-6, pp. 423–429, 1997.